Numerical Investigation of Mural Thrombus Formation in Stenosed Microvessels Using a Microfluidic Platform

MS (Research) Thesis

By

NIKHIL PANDEY

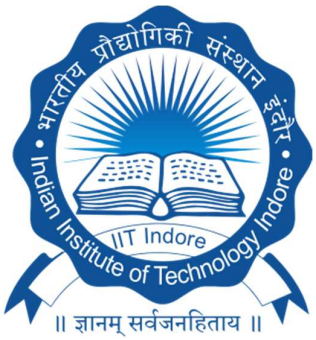

DEPARTMENT OF MECHANICAL ENGINEERING

INDIAN INSTITUTE OF TECHNOLOGY INDORE

JULY 2025

Numerical Investigation of Mural Thrombus Formation in Stenosed Microvessels Using a Microfluidic Platform

A THESIS

Submitted in fulfillment of the
requirements for the award of the degree
of

Master of Science (Research)

by

NIKHIL PANDEY

DEPARTMENT OF MECHANICAL ENGINEERING
INDIAN INSTITUTE OF TECHNOLOGY INDORE

JULY 2025

INDIAN INSTITUTE OF TECHNOLOGY INDORE

CANDIDATE'S DECLARATION

I hereby certify that the work which is being presented in the thesis entitled **Numerical Investigation of Mural Thrombus Formation in Stenosed Microvessels Using a Microfluidic Platform** in the fulfillment of the requirements for the award of the degree of **Master of Science (Research)** and submitted in the **Discipline of Mechanical Engineering, Indian Institute of Technology Indore**, is an authentic record of my own work carried out during the time period from July 2023 to July 2025 under the supervision of Dr. Vijai Laxmi, Assistant Professor, Indian Institute of Technology Indore.

The matter presented in this thesis has not been submitted by me for the award of any other degree of this or any other institute.

Nikhil

(Nikhil Pandey)

This is to certify that the above statement made by the candidate is correct to the best of my/our knowledge.

Vijai Laxmi

(Dr. Vijai Laxmi)

Nikhil Pandey has successfully given his MS (Research) Oral Examination held on 13th November 2025

14-11-2025
Signature of Chairperson (OEB) with date

Vijai Laxmi 14/11/2025
Signature(s) of Thesis Supervisor(s) with date

S. Jaheery 14-11-2025
Signature of Convener, DPGC with date

November 14, 2025
Prof. Shanmugam Dhinakaran
Signature of Head of Discipline with date

Acknowledgements

This work, titled "**Numerical Investigation of Mural Thrombus Formation in Stenosed Microvessels Using a Microfluidic Platform**", is not the result of my own efforts alone, it was possible because of all the named and unnamed people who helped me to shape my research and myself as an individual. I am indebted to many people.

First and foremost, I would like to express my sincere gratitude to my thesis supervisor, **Dr. Vijai Laxmi**, Assistant Professor, Department of Mechanical Engineering, IIT Indore, for her constant support, valuable guidance, and for nurturing my mind to complete this research work. Her mentorship has been a great guidance in shaping my academic journey.

I am deeply thankful to **Prof. I.A. Palani**, whose beautiful way of teaching and patience in addressing my countless questions during class played a crucial role in building my conceptual clarity and interest in the subject.

I am especially grateful to my seniors of Lab LG 10, Ms. Nisha Kumari, for her countless instances of help that made my journey at IIT Indore a success. Mr. Abhishek Singh, and Mr. Tejpratap Singh for their invaluable support. My heartfelt thanks to my lab mates and juniors, Prithviraj Soni, Bhaskar Anupam, Imon Jyoti, Vivek Kumar, Ritik Raj, Aditya Bindal, Nambiar Anand, and Sarang Jagdish for teaching me numerous significant things throughout this journey.

I would also like to acknowledge the Department of Mechanical Engineering and all the staff members of IIT Indore for their continuous support in my daily academic life.

Heartfelt appreciation to my seniors, roommates, hostel mates, and batch mates.

To all of you - Thank you from the bottom of my heart.

Dedicated

To

My mother, a strong and gentle soul who taught me to trust in God and believe in my work

Abstract

Vascular stenosis is the localized narrowing of blood vessels resulting from plaque accumulation along the vessel walls. Such constriction reshapes local flow patterns and alters local hemodynamics, promoting platelet activation and aggregation downstream. Over time, these disturbances can lead to the development of mural thrombus. In this study, we investigated the effect of geometrical variations within stenosed microvessels, including severity of stenosis, angular topology, curvature, and post-stenotic dilatation (PSD), on blood flow characteristics governing thrombus initiation. To investigate these effects, a combined experimental and computational approach was adopted. Microchannels were fabricated using stereolithography based 3D printing and soft lithography processes. The fabricated high-resolution, leak-proof microdevices were used for flow characterization. Subsequently, experiments were conducted on fabricated microchannel to validated the computational blood-flow model and accuracy of the computation approach. Following validation, extensive numerical simulations were performed over a wide range of geometrical configurations and flow conditions (bulk shear rates ranging from 100-30,000 s^{-1}) to examine flow behaviour. The analysis revealed that higher bulk shear rates intensified wall shear distribution and strengthened downstream recirculation. These behaviours resulted from increased inlet momentum, enhancing velocity gradients near the constriction and transferring greater tangential stress to the fluid layers adjacent to the wall. The resulting pressure drop across the stenosis induce flow separation and recirculation zones, increasing platelet residence time near the vessel wall. Prolonged exposure to such disturbed flow conditions increases the likelihood of platelets activation and aggregation. A three-quarters increase in stenosis severity creates nearly a 12-fold rise in velocity gradients at the throat. Consequently, platelets experienced extreme shear stresses capable of deforming their membranes and initiating activation pathways. Combined exposure to high shear at the throat and prolonged residence in post-stenotic low

shear regions established a hemodynamic environment favourable for thrombus initiation. Angular topology and curvature extend strong effect on local flow patterns and thrombogenic potential. Variations in inlet angle resulted minimal effect on mean shear, whereas sharper exit angles disrupted downstream flow. This strengthens vortices and shear gradients, leading to platelet trapping and adhesion. Smaller exit angles enabled smoother reattachment of streamlines, stabilizing downstream flow. A larger curvature radius at stenosis throat reduces abrupt velocity changes and shear, limiting platelet activation. However, outward displacement of recirculation zones toward the outer wall may still favour localized platelet deposition, suggesting curvature geometry governs the spatial distribution of thrombosis-prone regions.

In addition, analysis of complex vascular geometries, including multiple stenoses and post-stenotic dilatation (PSD), demonstrated repetitive flow acceleration and deceleration resulting in alternate high and low-shear regions. Platelets exposed to these oscillatory stresses experience cyclic deformation. Such mechanical loading increases platelet sensitivity to activation and adhesion. High intensity recirculation zones within the dilated downstream region extend platelet residence time, further promoting platelet aggregation under low-shear environment. The simultaneous exposure to elevated shear in the throat and prolonged residence in downstream low shear regions significantly enhances the risk of mural thrombosis.

Overall, this study provides a comprehensive understanding of the interplay between microvascular geometry and hemodynamic disturbances in mural thrombus formation. These findings can aid in developing predictive models for thrombotic risk analysis in cardiovascular diseases and improving the design of blood wettable medical devices.

List of Publications

Pandey N., Laxmi V., (2025), A Computational Fluid Dynamics Approach to Investigate the Development of Mural Thrombus in Microvessels with Stenotic and Poststenotic Dilatation Zones, Ind. Eng. Chem. Res., 64 (32), 15550-15561 (DOI: 10.1021/acs.iecr.5c01702)

Pandey N., Palani I. A., Laxmi V., (2024), "Development of Lab-on-Chip Device for Hemodynamic Study of Vascular Stenosis: Experimental and Numerical Investigation", Proceedings of 13th International Conference on Precision, Meso, Micro and Nano Engineering (COPEN 13).

Table of Contents

List of Figures

List of Tables

Acronyms

ADP	Adenosine diphosphate
Al	Aluminium
CF_4	Carbon tetrafluoride
CO_2	Carbon dioxide
CAD	Computer aided designs
CFD	Computational fluid dynamics
COC	Cyclic olefin copolymers
COP	Cyclic olefin polymers
CT	Computed tomography
ECM	Extra cellular matrix
EDTA	Ethylenediaminetetraacetic acid
$FeCl_3$	Ferric chloride
HF	Hydrofluoric acid
LoC	Lab-on-a-Chip
μPIV	Micro particle image velocimetry
NO	Nitric oxide
O_2	Oxygen
PC	Polycarbonate
PDMS	Polydimethylsiloxane
PMMA	Polymethyl methacrylate

PSD	Post-stenotic dilatation
KOH	Potassium hydroxide
PGED	Professional group on electron devices
RBCs	Red blood cells
RIE	Reactive ion etching
Rep rate	Repetition rate
NaOH	Sodium hydroxide
SOD	Stand off distance
SLA	Stereolithography
SF_6	Sulfur hexafluoride
3D	Three-dimensional
TXA2	Thromboxane A2
UV	Ultraviolet
vWD	von Willebrand disease
vWF	von Willebrand factor
WBCs	White blood cells

Chapter 1

Introduction

Microfluidics is the science of manipulating fluids at small scale. It had transformed various scientific fields through its ability to precisely control small volumes of fluids, preferably in the range of 10^{-9} to 10^{-18} liters. This technology has found its applications in areas such as analysis, chemical synthesis, separation, environmental monitoring, and biomedical diagnostics [1, 2]. Microfluidic devices have been widely used in various biomedical applications, including point-of-care diagnostics, drug discovery, and personalized medication. One notable application of this technology is in the investigation of circulatory disorders. By replicating the complex biological environment and flow conditions of the human vasculature, the microfluidic platform provides a controlled environment to study cardiovascular diseases, particularly atherosclerosis and thrombosis [3].

Thrombosis is the formation of blood clots within blood vessels. It is the leading cause of cardiovascular mortality worldwide, representing one-third of all global deaths. It often results from atherosclerosis, a condition characterized by the buildup of plaques within arterial walls. This development of atherosclerosis can cause vascular stenosis, the narrowing of blood vessels, which disrupts normal blood flow and contributes to thrombus formation [3, 4].

Vascular stenosis develops through a series of complex processes which is primarily initiated by endothelial dysfunction. This gradually leads to plaque formation, which narrows the blood vessels and disrupts normal circulation, as can be seen from Figure 1.1 [5, 6]. This narrowing alters hemodynamic parameters, such as velocity, flow patterns, formation of recirculation zones, pressure gradient, and shear stress. These abnormal flow conditions create an environment that promotes platelet activation and their aggregation at sites of disturbed flow [7]. High shear rates, particularly in stenotic regions, enhance the secretion of prothrombotic

agents like adenosine diphosphate (ADP) and thromboxane A2 (TXA2) and enhance their interaction with von Willebrand factor (vWF). This facilitates platelet aggregation and initiates thrombus formation [8]. Similar effects can also be experienced by medical implants such as heart valves, stent placement, or injury in the vascular network.

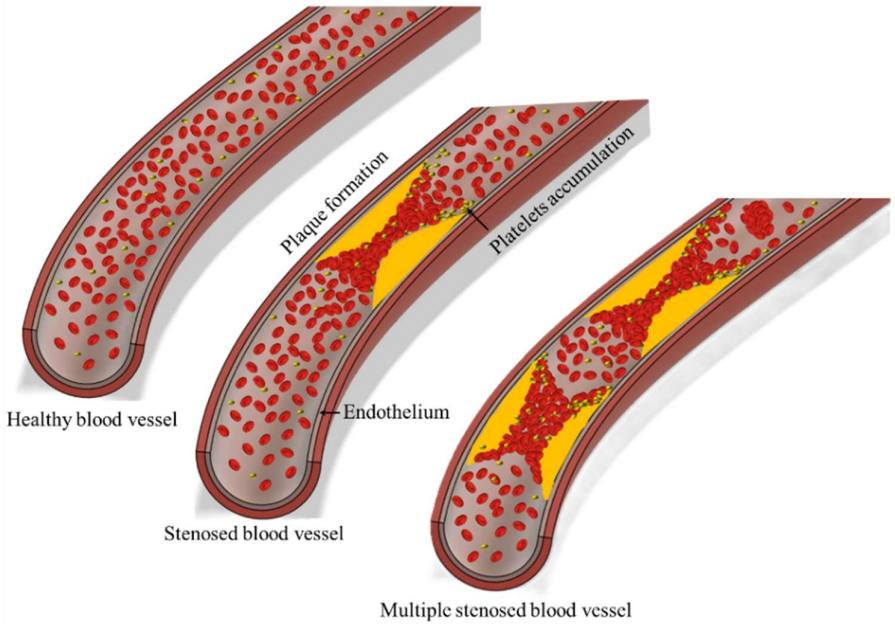

Figure 1.1: Illustration showing healthy and stenosed blood vessels comparing normal blood flow with disturbed flow due to plaque buildup.

The growing use of blood-wetted medical devices drives the need for a better understanding of thrombus formation. These devices often create an environment of non-physiological shear, disturbed flow patterns, and bring blood in contact with foreign surfaces. Such factors can lead to complications such as haemolysis and thrombosis, presenting a complex challenge for the designers of such devices [9]. The scale of severity increases with the presence of multiple stenosed regions. A few studies in the literature [10-12] have explored the effect of fluid dynamics and geometrical features influence in cases involving multiple stenoses and post-stenotic dilatation (PSD) regions, which results in the development of thrombus. Therefore, in this thesis, we have investigated the combined effect of geometrical and hemodynamic parameters in various

stenosis geometries and further investigated the blood flow dynamics of single, multiple stenosed microvessels and microvessels with post-stenotic dilatation on the development of mural thrombosis, in detail. The outcomes of the present study will make a foundation for modelling vascular stenosis, drug development, and designing better medical devices and implants.

We have structured this thesis to systematically investigate the effect of varying severities of vascular stenosis. The following sections detail the computational and experimental setup, followed by the analysis performed, and a summary of the key findings. In chapter 2, the background of thrombosis, along with a review of existing research, forms the foundation of the problem statement. Chapter 3 outlines the fundamental equations and simulation methodology used in further study. Chapter 4 provides a comprehensive overview of different materials and methods used in microfluidic device fabrication, with the focus on implementing three-dimensional (3D) printing method for the present work. In chapter 5, we investigated the hemodynamic variations due to changes in the geometry of the stenosed region. Chapter 6 focuses on hemodynamic effects of healthy, single stenosis, multiple stenoses, and PSD regions occurring in series, offering insights into their impact on flow disturbance and the possibility of clot formation. Lastly, chapter 7 highlights the key findings of the present work, and suggests future research directions that could help to enhance the understanding of vascular disorders.

Chapter 2

Review of Literature

2.1 Overview of thrombosis and the key cause of clot formation

Haemostasis is a natural physiological process through which the body prevents excessive blood loss by forming clots at the site of vascular injury. It plays an essential role in controlling bleeding and tissue repair. In a healthy state, this mechanism is regulated to ensure rapid clot formation at the site of injury, while minimizing the risk of unnecessary clot development [13]. When this balance is disrupted, it can result in thrombosis, abnormal formation of a blood clot, commonly known as thrombus, within the blood vessels of the circulatory system. This often leads to obstruction in normal blood flow, which could potentially give rise to life-threatening conditions such as myocardial infarction (heart attack), ischemic strokes (blockage of blood flow to the brain), deep vein thrombosis (typically in legs, thighs, or pelvis), or pulmonary embolism (blockage in the arteries of lungs) [14].

Among the various factors associated with the thrombus formation, lifestyle-related factors such as smoking, diabetes, hypertension, or physical inactivity are widely recognized as major contributors [5]. These factors are commonly known to induce endothelial dysfunction and chronic inflammation within the blood vessels. Damaged or inflamed endothelium loses its ability to regulate blood flow, inflammatory responses, and prevent abnormal clot formation, which creates a pro-thrombotic environment [15]. The underlying mechanisms of thrombus formation are commonly described by Virchow's triad, a fundamental concept named after the German physician Rudolf Virchow. This triad describes the three broad categories of factors that contribute to thrombus formation: endothelial injury/dysfunction, hypercoagulability, and hemodynamic changes [4]. These mechanisms

often work together with lifestyle-related factors, initiating vascular damage and inflammation, giving rise to disturbed flow conditions and promoting clot formation. Understanding these interconnected processes is essential for improving the prevention, diagnosis, and treatment of thrombotic diseases.

2.2 Virchow's triad

In 1856, Rudolf Virchow introduced the foundational principle for studying thrombus formation, which is now referred to as Virchow's triad [16]. The triad interlinks the dysfunction of surface bounding the flow (endothelial injury/dysfunction), to the chemical and cellular components of blood associated with clot formation (hypercoagulability), and the abnormalities in the blood flow (hemodynamic changes), as shown in Figure 2.1 [17]. These elements often work together, which creates conditions favourable for clot formation within the circulatory system [4].

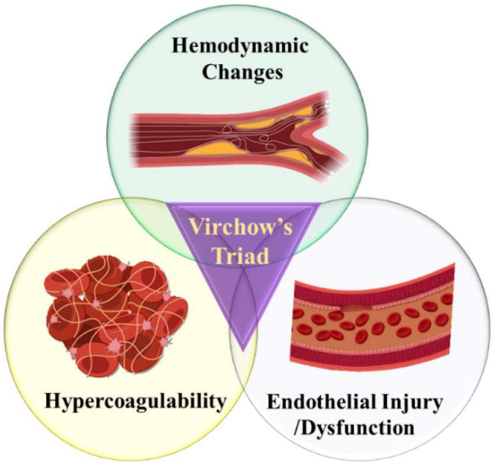

Figure 2.1: Virchow's triad showing the bridge between three major factors contributing to thrombus formation [17].

2.3 Endothelial injury or dysfunction

Among the three principles of Virchow's triad, endothelial injury or dysfunction plays a critical role in the process of thrombus formation. Blood vessels, which include arteries, veins, and capillaries, form a

network responsible for transporting blood and nutrients through the body. Structurally, both arteries and veins share a common arrangement consisting of three distinct layers: the adventitia (tunica externa), the tunica media, and the tunica intima [18], as shown in Figure 2.2 [17]. The adventitia, which is the outermost layer, consists of connective tissue, provides mechanical strength. Then is the intermediate layer - tunica media, which is composed of extracellular matrix and smooth muscle cells, allowing vessels to stretch and contract to regulate blood flow and varying pressure. Finally, the innermost layer, the tunica intima, comprises of monolayer of endothelial cells [19].

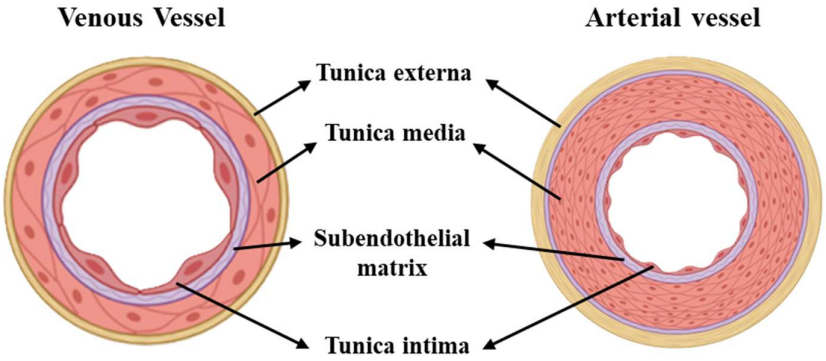

Figure 2.2: Schematic representation of different layers of venous and arterial vessels [17].

The endothelial cellular layer is not only a passive lining of blood vessels but an active interface which forms a barrier to provide unobstructed blood flow. It also mediates the exchange of nutrients between blood and surrounding tissues and plays a central role in maintaining vascular inflammatory responses, inappropriate clot formation [20]. Endothelium dysfunction occurs when this protective balance is disrupted due to an increase in free radicals. This can disrupt the balance of nitric oxide (NO), injure the endothelial lining, and allow toxins to pass into body tissues. Various factors contribute to elevated production of free radicals in the body, such as smoking, high glucose intake, obesity, microbial infections, exposure to metals, and environmental pollutants [5].

As the endothelial layer becomes permeable, allowing inflammatory mediators and circulatory proteins to pass into the surrounding tissue, causing local inflammation and disruption of endothelial function [5]. This process further attracts different immune cells like monocytes, T cells, and platelets to the affected area. Monocytes further migrate into the sub-endothelium and transform into foam cells, forming fatty streaks, which further promote the deposition of lipids and proteins within the arterial wall, gradually leading to plaque formation [21]. As plaques grow, they progressively narrow the vessel lumen and disturb the normal flow, leading to formation of recirculation regions and disturbed hemodynamic conditions. These disturbances further damage the endothelium and promote platelet activation. Understanding how these altered flow patterns affect clot formation and growth is essential for comprehending the complex interplay between vascular pathology and thrombosis [22]. The following section explores the underlying fluid mechanics of blood clot formation and examines the contribution of hemodynamic parameters in thrombus initiation and propagation.

2.4 Fluid mechanics of thrombus formation

As the atherosclerotic plaque develops within the arterial wall, it gradually changes the geometry of the blood vessel, which causes significant disturbances to the normal flow of blood. When the vessel lumen narrows, the available cross-section area for blood flow reduces, which increases the blood velocity as per the principle of conservation of mass. This increase in velocity results in amplification of shear stress acting on the vessel wall and edges of the plaque. Additionally, this abrupt geometric narrowing creates adverse pressure gradients, which lead to flow separation and formation of recirculation zones in the downstream of stenosis. These localized disturbances in flow create areas of low or oscillating shear, which are well known to promote pro-thrombotic conditions [23, 24].

Another phenomenon which affects the thrombus formation is platelet margination. Under normal flow conditions, red blood cells (RBCs),

which are deformable in nature, migrate towards the center of the blood vessel, causing the platelets to move towards the vessel wall. This phenomenon ensures that the platelets remain in close proximity to vessel lining and can readily respond to vessel wall injury or dysfunction [25, 26]. In the narrowed region, the increased shear further enhances platelet interactions with the vessel wall and plaque surface, assisting their adhesion to injured or activated endothelium. Among the various mediators of platelet adhesion in high shear conditions, vWF plays a key role [27]. Under low shear conditions, vWF remains in a compact, globular form with limited interaction. However, when exposed to high shear conditions, they undergo unfolding and transport towards the vessel wall through diffusivity. This high shear condition leads to formation of elongated vWF net near the plaque surface. Upon unravelling, vWF exposes certain binding sites where platelet receptors such as GPIb-IX-V complex interact, thus initiating platelet adhesion under disturbed flow conditions. As time progresses, this vWF forms a multilayer fibrous network that helps in trapping circulating platelets and further supports thrombus growth [28].

Following adhesion, platelet undergoes activation, a process through which platelets transform from smooth disc-like cells into irregular-shaped structures. This morphological transformation increases the surface area of platelets, allowing for more adhesion receptors to become exposed and facilitating enhanced attachment to both vessel wall and nearby platelets [29]. Activated platelets also secrete various chemical mediators such as ADP, TXA2, and additional vWF. These mediators recruit additional circulating platelets at the site of injury, thus facilitating thrombus growth. Moreover, this platelet activation induces a structural change in platelet integrins (receptor proteins found on platelet surface) such as $\alpha IIb\beta_3$, which promotes platelet-platelet interaction and stabilizes the clot formed [30].

As the thrombus grows, it distorts the local flow field, producing shear gradients, creating stagnation flow and recirculation zones around its structure. These altered flow patterns increase the residence time of

clotting factors, thus promoting additional platelet activation. The development of thrombus in areas of plaque-induced narrowing results from the combined influence of vascular geometry changes, hemodynamic disturbances, and flow-responsive biological processes [31, 32]. This interplay of fluid mechanics, biochemical signalling, and cellular interaction is crucial in understanding the mechanism of thrombus formation for development of improved blood-wettable medical devices, drugs, personalized mediation, etc.

2.5 Comprehensive review of existing research on vascular stenosis and thrombus formation

Several studies [7, 10, 33-50] have highlighted the role of various flow dynamic parameters including pressure gradient, flow velocity changes, shear rate and its gradient variation, wall shear stress, and recirculation zones in initiating and progression of thrombus. Young et al. (1973) experimentally investigated steady flow through stenosed models, focusing on pressure difference, flow separation, and turbulence. They found that severity of stenosis greatly affects these parameters, with severe narrowing causing more turbulence and pressure drop. Bluestein et al. (1997) investigated the relationship between disturbed flow dynamics in stenosed arteries and the development of mural thrombus using computational simulation and experimental validation. This is done using an axisymmetric stenosed model with 84% area reduction at the Re ranging from 300 to 3,600. Their results demonstrated that high-velocity jets formed at the narrowed region create recirculation zones with low and oscillating shear downstream. They showed that platelet activation occurs at high shear stresses at the stenosis throat, whereas its adhesion predominantly occurs in the low-shear recirculation zones. Schneider et al. (2007) showed that vWF factor undergoes a structural change from a collapsed compact shape to stretched form when exposed to high shear rates. Through experiments and simulations, the authors demonstrated that this unfolding promotes vWF to support platelet adhesion in high shear environments. Nesbitt et al. (2009) showed that platelet aggregation during thrombus formation is not only driven by

soluble agonists but also depends on blood flow dynamics. By using high-resolution intravital imaging techniques and flow analysis, the authors found that platelets adhere in a low-shear region downstream of the stenosed region. The stability of these aggregates depends on membrane tether restructuring. Their finding highlights the central role of shear gradients in driving thrombus growth and platelet aggregation. Tovar-Lopez et al. (2011) developed a computational model to simulate blood flow in stenosed arterioles of mice. They investigated the role of local shear gradients and flow acceleration or deceleration in platelet activation, demonstrating that platelet activation depends not only on chemical activators but also on the mechanical effects of microscale shear gradients. Their study also identified a correlation between vessel wall property and hemodynamic flow, suggesting that critical acceleration and deceleration of blood flow at the site of stenosis are influenced by tissue elasticity. Westein et al. (2013) used a semi-circular channel of varying degree of stenosis to demonstrate how plaque geometries affect local blood flow patterns, particularly in the downstream of the stenotic region that promotes platelet aggregation. This is due to increased accumulation of vWF at these sites. They showed that thrombus formation is more noticeable in the outer region of stenosis. Their findings highlighted that vWF is a key mediator which links altered shear environments to pathological thrombus formation in stenosed blood vessels. Ha et al. (2013) experimentally examined the effect of disturbed flow caused by stenosis on platelet aggregation in an 85% stenosed microchannel with trapezoidal geometry. Using micro particle image velocimetry (μPIV), they mapped flow patterns and identified recirculation zone formation in the downstream of stenosis across the flow rate range of 10 mL/hr to 50 mL/hr. Platelet aggregation was found to occur at the interface between central jet and recirculating flow, highlighting the relation between local hemodynamic disturbances and platelet aggregation patterns. The recirculation zones coincide with the platelet-rich and RBC-deficient regions. Ciciliano et al. (2015) developed a microfluidic system to investigate how ferric chloride ($FeCl_3$) induces thrombosis. They showed that $FeCl_3$ triggers blood

component aggregation through charge-based interactions, not through traditional biological receptors. At first positively charged iron ions bind to negatively charged cells and proteins, causing initial aggregation, followed by the typical clotting processes of platelet activation and fibrin formation. This study showed that $FeCl_3$ concentrations are key to clot formation. Jain et al. (2016) developed a microfluidic device to mimic a stenosed arteriolar network. This device monitors the whole blood coagulation and platelet function under physiologically relevant shear gradients. The device integrates shear-activated clotting mechanisms and uses a mathematical model to quantify clotting time from pressure changes due to channel occlusion. It enables real-time assessment of haemostasis using low volume of blood, proving its potential for personalized diagnostics and monitoring of antithrombotic therapy. Brazilek et al. (2017) have developed a microfluidic device designed to generate strain rate gradients to initiate platelet aggregation for von Willebrand disease (vWD) screening. Their platform provides rapid and high-throughput for diagnosing vWD and other shear-dependent disorders. Costa et al. (2017) developed a 3D-printed microfluidic model that closely mimics the real structure of human arteries, both healthy and stenotic. This device was created using computed tomography (CT) angiography data and stereolithography (SLA). These realistic vessel geometries were cast into polydimethylsiloxane (PDMS) to create transparent microfluidic chips, which were lined with human endothelial cells. Blood perfusion experiments showed that thrombosis occurred only in the stenotic models, especially near and downstream of the narrowed regions. Ting et al. (2019) introduced a microfluidic method to measure the contractile force generated by platelet aggregates under shear conditions. Their results showed that platelet force decreases with antiplatelet drugs, particularly in patients taking aspirin. Their work also provides an insight into developing an approach for monitoring antiplatelet therapy and assessing the risk of traumatic bleeding. Receveur et al. (2019) utilized a stenosed channel to demonstrate the influence of shear rate gradients in transforming weakly adhesive proteins into thrombogenic

surfaces. Menon et al. (2020) presented a circular stenosed model mimicking the arterial narrowing to study disturbed hemodynamic and endothelial dysfunction. They demonstrated the presence of high shear stress in the stenosed area and recirculating flow formation in the downstream of stenosis. Drug testing with antithrombotic agents validated the clinical relevance of this platform. Berry et al. (2021) developed a microfluidic device that generates occlusive thrombi under arterial shear using human whole blood. This device features a branching channel with pressure relief and an ethylenediaminetetraacetic acid (EDTA) quenching system to prevent downstream coagulation. They introduced a robust approach to measure occlusion time by monitoring flow rate. The platform allows dose-dependent assessment of platelet inhibitors and offers a robust tool for preclinical screening of antithrombotic therapies using human blood. Zhao et al. (2021) developed a refined CFD approach to model the effect of bulk flow rate on hemodynamic parameters such as shear rate gradient and wall shear stress for low flow rate (i.e., 1.84 μL/min to 36.77 μL/min). Zainal Abidin et al. (2022) developed a microfluidic model to study how platelets respond to rapid changes in blood flow, especially under conditions like severe vessel narrowing. Their findings revealed that platelets can sense and respond to extensional strain, a stretching force in the flow, without physical contact with vessel walls or binding to adhesive proteins. This response is mediated by a newly identified mechanosome inside platelets, which initiates calcium entry in platelets, an early step in clot formation. Unlike traditional views, this activation does not depend on adhesion or chemical agonists. Flores Marcial et al. (2022) visualized thrombosis formation in microchannels containing one, two, or three stenoses using whole blood where thrombus growth was consistently initiated at the first stenosis. Ham et al. (2023) combined multiphase CFD and microfluidic experiments to examine thrombus formation. They simulated blood as a two-phase mixture of plasma and RBC, focusing on the distribution of shear stress and plasma, highlighting critical regions that affect clot growth. Zhang et al. (2023) designed a microvasculature-on-a-post chip to model how blood clots

form in vessels with partial stenosis. The chip contains 3D micro posts of varying sizes that disturb blood flow and simulate different degrees of vascular blockage. These structures were coated with endothelial cells and perfused with human blood to mimic real vessel conditions. The study showed that disturbed flow and inflammation significantly change endothelial behavior and promote clot formation in downstream regions. Thrombus composition (platelets and fibrin) varied depending on the post size and flow disturbance. This chip replicates all three aspects of Virchow's Triad (hemodynamic changes, hypercoagulability, and endothelial dysfunction) and offers a new approach for studying thrombosis and testing antithrombotic therapies.

The preceding literature survey provided a comprehensive overview of the influence of various hemodynamic factors such as pressure difference, velocity distribution, wall shear stress, shear rate, and its gradient on thrombus development. While limited studies have investigated the effect of blood flow dynamics and geometrical configuration of stenosed region on the wall-induced thrombus formation. The present work further examines flow behavior in healthy, multiple stenosed, and stenoses with PSD microvessels that may lead to mural thrombus formation. A comprehensive understanding of the hemodynamics in such microvascular conditions can significantly enhance the existing literature for various applications in the biomedical fields, such as the development of improved blood-wettable medical devices, drugs, personalized medication, etc.

Chapter 3

Methodology of Investigation

This section outlines a detailed overview of the methodology used in our study. It involves the formulation of fundamental governing equations, and the application of appropriate boundary conditions to investigate the blood flow dynamics in stenosed microvessels. The computational approach used is validated by comparing the simulation result with analytical and experimental data. This has been done to establish the accuracy and reliability of our computational methodology for further analysis in various microvascular geometries. All numerical investigations have been done using COMSOL Multiphysics software.

3.1 Numerical methodology

3.1.1 Governing equations

In this study, we have performed numerical investigation of blood flow on the microvascular geometries. The blood flow is mathematically described by using two fundamental equations, the continuity equation (Eq. 1), which is associated with conservation of mass, and the Cauchy momentum equation (Eq. 2), which accounts for the balance of forces acting on the fluid and is fundamentally associated with conservation of momentum [51]. The momentum equation is further expressed in its component form along the x, y and z directions as shown in Eq. 2a, 2b and 2c respectively. Throughout our simulations, we have assumed the blood flow to be laminar and incompressible across the entire domain.

$$\frac{\partial u}{\partial x}+\frac{\partial v}{\partial y}+\frac{\partial w}{\partial z}=0 \qquad \text{(Eq. 1)}$$

$$\rho\left(\frac{\partial u_i}{\partial t}+u_j\frac{\partial u_i}{\partial x_j}\right)=-\frac{\partial P}{\partial x_i}+\frac{\partial \tau_{ij}}{\partial x_j} \qquad \text{(Eq. 2)}$$

x momentum:

$$\rho\left(\frac{\partial u}{\partial t}+u\frac{\partial u}{\partial x}+v\frac{\partial u}{\partial y}+w\frac{\partial u}{\partial z}\right)=-\frac{\partial P}{\partial x}+\frac{\partial \tau_{xx}}{\partial x}+\frac{\partial \tau_{xy}}{\partial y}+\frac{\partial \tau_{xz}}{\partial z} \qquad \text{(Eq. 2a)}$$

y momentum:

$$\rho\left(\frac{\partial v}{\partial t}+u\frac{\partial v}{\partial x}+v\frac{\partial v}{\partial y}+w\frac{\partial v}{\partial z}\right)=-\frac{\partial P}{\partial y}+\frac{\partial \tau_{yx}}{\partial x}+\frac{\partial \tau_{yy}}{\partial y}+\frac{\partial \tau_{yz}}{\partial z} \qquad \text{(Eq. 2b)}$$

z momentum:

$$\rho\left(\frac{\partial w}{\partial t}+u\frac{\partial w}{\partial x}+v\frac{\partial w}{\partial y}+w\frac{\partial w}{\partial z}\right)=-\frac{\partial P}{\partial z}+\frac{\partial \tau_{zx}}{\partial x}+\frac{\partial \tau_{zy}}{\partial y}+\frac{\partial \tau_{zz}}{\partial z} \qquad \text{(Eq. 2c)}$$

where u, v, w represents the velocity components (m/s) in x, y, z direction respectively, ρ is the density (kg/m^3) with the value of 1060 kg/m^3 for blood, P is the blood pressure (Pa), and τ_{ij} is the viscous stress tensor as per Eq. 3:

$$\tau_{ij}=\mu(\dot{\gamma})\left(\frac{\partial u_i}{\partial x_j}+\frac{\partial u_j}{\partial x_i}\right) \qquad \text{(Eq. 3)}$$

so explicitly:

$$\tau_{xx}=2\,\mu(\dot{\gamma})\frac{\partial u}{\partial x}, \tau_{yy}=2\,\mu(\dot{\gamma})\frac{\partial v}{\partial y}, \tau_{zz}=2\,\mu(\dot{\gamma})\frac{\partial w}{\partial z}$$

$$\tau_{xy}=\mu(\dot{\gamma})\left(\frac{\partial u}{\partial y}+\frac{\partial v}{\partial x}\right), \tau_{yz}=\mu(\dot{\gamma})\left(\frac{\partial v}{\partial z}+\frac{\partial w}{\partial y}\right), \tau_{zx}=\mu(\dot{\gamma})\left(\frac{\partial w}{\partial x}+\frac{\partial u}{\partial z}\right)$$

where μ indicates the dynamic viscosity (Pa s), and $\dot{\gamma}$ reflects the shear rate of flow.

Blood is a highly complex fluid; accurate modelling of its flow using any standard computational platform presents significant challenges. Some of these challenges include high computational costs and complexity in capturing intricate properties between cells and other components. In general, blood consists of various cellular components such as red blood cells (RBCs), white blood cells (WBCs), and platelets suspended in protein-rich plasma fluid. Among these, RBCs particularly influence the rheological properties of blood. They account for about 45% of blood by volume, a measure commonly referred to as haematocrit [52]. Unlike other cells, RBCs are deformable in nature, and this behavior under various flow conditions plays a crucial role in altering the viscosity of blood. According to literature, when blood flows through vessels, which typically have a diameter of less than 300 μm, a

phenomenon of Fåhræus-Lindqvist effect comes into play. Due to this phenomenon, RBCs tend to move towards the center of the vessel, which creates a cell-free plasma layer near the vessel walls [53]. This redistribution of RBCs results in a reduction of the apparent viscosity of blood; therefore, the blood shows both Newtonian and non-Newtonian behavior where viscosity decreases with an increase in bulk shear rate, and it later approaches a constant value of infinite-shear rate viscosity.

We have explored a variety of viscosity models based on fitting constants to commonly known equations. These models have been used to simulate the shear-thinning behavior of blood flow. A few of the commonly used models are Power Law [54], Generalized power law [55], Casson model [56], Cross model [57], K-L model [54], Carreau model [58], Carreau Yasuda model [59], Population balance-based thixotropic model [60], Population balance blood model [61], Viscoelastic models [62, 63], Mixture theory model [64] etc. The relationship between viscosity and the shear rate, and values of coefficients from different literature are listed in Table 1.

Table 1: Different viscosity models for blood taken from the literature.

Model	Equation	Coefficients
Power Law [54]	$\mu = k(\dot{\gamma})^{n-1}$	$k = 0.017$ $n = 0.708$
Generalized power Law (GP) [55]	$\mu = k(\dot{\gamma})^{n-1}$ $k = k_\infty + \delta k\, exp\left(-\left(1+\frac{\dot{\gamma}}{a}\right) exp\left(\frac{-b}{\dot{\gamma}}\right)\right)$ $n = n_\infty - \delta n\, exp\left(-\left(1+\frac{\dot{\gamma}}{c}\right) exp\left(\frac{-d}{\dot{\gamma}}\right)\right)$	$k_\infty = 0.0035\ Pa\ s$ $\delta k = 0.025$ $n_\infty = 1$ $\delta n = 0.45$ $a = 50$, $b = 3$ $c = 50$, $d = 4$
Casson model [56]	$\mu = \left(\sqrt{\mu_c} + \sqrt{\tau_c/\dot{\gamma}}\right)^2$	$\mu_c = 0.00414\ Pa\ s$ $\tau_c = 0.0038\ Pa$
Cross model [57]	$\mu = \mu_\infty + (\mu_0 - \mu_\infty)(1 + (\lambda\dot{\gamma})^2)^{-n}$	$\mu_\infty = 0.0035\ Pa\ s$ $\mu_0 = 0.0364\ Pa\ s$ $\lambda = 0.38$, $n = 1.45$

K-L model [54]	$\mu = \frac{1}{\dot{\gamma}}\left(\tau_c + \mu_c\left(\alpha_1\sqrt{\dot{\gamma}} + \alpha_2\dot{\gamma}\right)\right)$	$\tau_c = 0.005\ Pa$ $\mu_c = 0.0035\ Pa\ s$ $\alpha_1 = 1.19523$ $\alpha_2 = 1$
Carreau model [58]	$\mu = \mu_\infty + (\mu_0 - \mu_\infty)(1 + (\lambda\dot{\gamma})^2)^{\frac{n-1}{2}}$	$\mu_\infty = 0.00345\ Pa\ s$ $\mu_0 = 0.056\ Pa\ s$ λ = 3.313 s n = 0.3568
Carreau Yasuda model [59]	$\mu = \mu_\infty + (\mu_0 - \mu_\infty)(1 + (\lambda\dot{\gamma})^a)^{\frac{n-1}{a}}$	$\mu_\infty = 0.0035\ Pa\ s$ $\mu_0 = 0.16\ Pa\ s$ λ = 8.2, n = 0.2128 a = 0.64

In this work, to accommodate and compare the effect of Newtonian and non-Newtonian behavior in computational simulations of microvessels, we have considered Carreau viscosity model, as given by Eq. 4.

$$\mu = \mu_\infty + (\mu_0 - \mu_\infty)(1 + (\lambda\dot{\gamma})^2)^{\frac{n-1}{2}} \quad \text{(Eq. 4)}$$

where μ is the viscosity as a function of the shear rate $\dot{\gamma}$ (s^{-1}), μ_∞ is the viscosity at high shear rate (low viscosity limit) (0.00345 Pa s), μ_0 is the viscosity at low shear rate (high viscosity limit)(0.056 Pa s), λ is the characteristic time constant (3.313 s), and n is the flow behavior index (0.3568). The Carreau model is a generalized form of a Newtonian fluid model that effectively captures the shear-dependent viscosity variations. At low shear rates, the fluid exhibits shear-thinning behavior, and later for higher shear rates, the fluid approaches a constant viscosity. This is particularly the case when the power-Law index n < 1. As reported in literature [65-69], several researchers have used the Carreau viscosity model to study blood flow through constricted microvessels. Further, we applied a fully developed volumetric flow rate Q (m^3/s) [Eq. 5] at the inlet. This assumes that the velocity profile of the fluid remains steady and well defined upon entering the domain. A no-slip boundary condition is applied along the inner wall of vessels, and a zero-gauge pressure boundary condition is implemented at the outlet. Together, these boundary conditions help in simulating blood flow within the microchannels.

$$\bar{\gamma}_{\beta} = \frac{Q\,\lambda}{2\,A\,D_h} \qquad \text{(Eq. 5)}$$

where A is the cross-sectional area at the inlet (m^2), D_h is the hydraulic diameter (m), $\bar{\gamma}_{\beta}$ is the bulk shear rate (s^{-1}), and λ is the shape factor of the microvessel [70], [71].

$$\lambda = \frac{24}{[(1-0.351Z_0/Y_0)(1+Z_0/Y_0)]^2} \quad \text{for} \frac{Z_0}{Y_0} \leq 1 \qquad \text{(Eq. 6)}$$

where Y_0 = 200μm represents the width of the microchannel. Z_0 = 100μm corresponds to channel depth.

In addition, as platelets travel through stenosed regions of microvessels, they are subjected to compression and stretching. This is due to acceleration of fluid particles in converging regions and deceleration in diverging regions. We have used elongational rate ($\dot{\varepsilon}$) to quantify this mechanical deformation [34], which measures the stretch of fluid element along the flow direction. Mathematically, this quantity can be calculated as the velocity gradient along the length of the microvessel as shown in Eq. 7. This parameter plays a crucial role in understanding platelet activation levels, particularly under disturbed flow conditions.

$$\dot{\varepsilon} = \frac{\partial u}{\partial x} \qquad \text{(Eq. 7)}$$

where u is the velocity along the length of the microvessel.

As the flow rate increases in the stenosed microvessel, altered geometry can cause the fluid streamlines to separate in the downstream of the narrowed region. This leads to the formation of recirculation zones, where the flow reverses and circulates in vortices. In this study, these zones are of particular interest because they can act as a trapping region for platelets and other blood components. This promotes local interaction that may lead to their activation. We have quantified the strength of these recirculation zones by calculating circulation (Γ), which measures the total rotational motion of the fluid over a defined surface. Here we are calculating circulation at the surface passing

through the middle of height (Z_0) of the microvessel. This parameter is mathematically expressed as per Eq. 8.

$$\Gamma = \iint \left(\frac{\partial v}{\partial x} - \frac{\partial u}{\partial y}\right) dA \qquad \text{(Eq. 8)}$$

3.1.2 Computational methodology

To begin with the establishment of computational methodology, we performed simulations on a straight channel with a rectangular cross-section, having dimension 200 µm × 100 µm and length 36.5 mm, as show in Figure 3.1.

The flow behavior within the channel was analyzed by solving the governing equations, along with the application of boundary conditions as we have discussed in section 3.1. These simulations were performed across a range of flow rates, each corresponding to different bulk shear rates as given in Table 3. For each case, we have calculated the pressure drop between the inlet and outlet, and the results are plotted in Figure 3.2 (a).

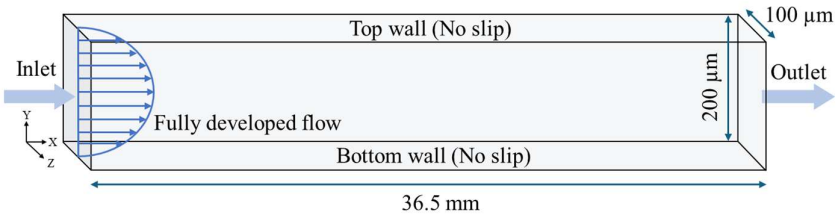

Figure 3.1: Illustration of computational domain highlighting the channel geometry and associated flow conditions.

To verify the accuracy of the computational model, we performed analytical calculations of pressure drop using the established fluid mechanics correlations for channels with rectangular cross-section.

3.1.3 Analytical validation

When analyzing the fully developed laminar flow in channels, the general principle remains similar to those applied in circular pipes or for

noncircular cross-sections such as rectangular or elliptical geometry. However, the algebra involved becomes significantly more complex due to the asymmetrical shape and variation in boundary conditions [72]. We can solve continuity and momentum equations for laminar flow and the head loss due to friction (h_f) for noncircular channels is defined by Eq. 9 [72].

$$h_f = \frac{\Delta p}{\rho g} + \Delta z = \frac{\bar{\tau}_a \, \Delta L}{\rho g \, A/\mathcal{P}} \quad \text{(Eq. 9)}$$

where Δp is the pressure drop (Pa) over the length of ΔL(m), Δz is the vertical distance between two ends of the channel (m), $\bar{\tau}_a$ is the average value of shear stress integrated around the perimeter (Pa), A is the cross-sectional area (m^2), $\mathcal{P}$ is the wetted perimeter (m).

For horizontal channels, the elevation head term (Δz) becomes zero, this simplifies the head loss to depend on pressure variation over the length of channel. Since the cross-section is not circular, the concept of pipe radius (R) is replaced by the hydraulic radius (R_h). This hydraulic radius is defined as the ratio of the cross-sectional area (A) to the wetted perimeter ($\mathcal{P}$), as given by Eq. 10.

$$R_h = \frac{A}{\mathcal{P}} \quad \text{(Eq. 10)}$$

In the fluid flow analysis, shear stress along the channel walls is generally considered as an average value. This helps provide a practical approximation of frictional effects. The friction factor in terms of average shear ($\bar{\tau}_a$) is shown by Eq. 11.

$$f = \frac{8 \, \bar{\tau}_a}{\rho \, V^2} \quad \text{(Eq. 11)}$$

Substituting the value of friction factor from Eq. 11 in Eq. 9, we get the relation between head loss and friction factor, which is defined as by Eq. 12

$$h_f = \frac{f \, L \, V^2}{4 \, R_h \, 2g} \quad \text{(Eq. 12)}$$

In engineering practice, the hydraulic diameter (D_h) is frequently used, it is defined as:

$$D_h = \frac{4A}{\mathrm{P}} = \frac{4 \times cross-sectional\ area}{wetted\ perimeter} = 4R_h \qquad \text{(Eq. 13)}$$

This definition standardizes the analysis of noncircular ducts by equating them to circular pipes of equivalent hydraulic behavior

$$h_f = \frac{\Delta p}{\rho g} = \frac{f\, L\, V^2}{D_h\, 2g} \qquad \text{(Eq. 14)}$$

For channels with a rectangular cross-section, friction factor and flow characteristics depend on the aspect ratio $\left({}^{b}/_{a}\right)$, where a and b represent the height and width of the rectangular cross-section [72]. Table 2 represents the product of friction factor and Reynolds number for various values of aspect ratio. We can use these values to compute pressure drops and head losses in rectangular microchannels under laminar flow conditions.

Table 2: Laminar friction constant $f\ Re_{D_h}$ for rectangular cross-section.

aspect ratio $\left({}^{b}/_{a}\right)$	$f\ Re_{D_h}$
0.0	96.00
0.1	84.68
0.25	72.93
0.5	62.19
0.75	57.89
1	56.91

Considering a rectangular microchannel with an aspect ratio of 0.5, the Reynolds number is defined as:

$$R_e = \frac{\rho\, V\, D_h}{\mu} \qquad \text{(Eq. 15)}$$

where $V = \frac{Q}{A}$ is the average velocity

Substituting these expressions into Eq. 14, we get the resulting pressure drop across the microchannel of length L as:

$$\Delta p = \frac{31.095\,\mu\,Q\,L}{A\,{D_h}^2} \qquad \text{(Eq. 16)}$$

This formulation captures the dependence of pressure drop on geometric parameters (such as aspect ratio), flow rate, and fluid properties. We have calculated the pressure drop across the rectangular channel using Eq. 16 for various flow rates listed in Table 3. The results are illustrated in Figure 3.2 (a).

To experimentally validate the computational methodology adopted in this study, we fabricated a microfluidic device and measured the pressure drop across the channel length.

3.2 Experimental methodology

The experimental procedure began with the fabrication of a microchannel designed to replicate the computational geometry, having a rectangular cross-section of 200 μm × 100 μm with a length of 36.5 mm. We explored a few cost-effective fabrication methods to fabricate the microfluidic device. Initially, we used CO_2 laser machining to create the channel on a silica glass slide and PDMS block. Although this method provided quick prototyping, we found limitations in precision and resolution of fabricated channels. To overcome these issues we adopted vat-polymerization based SLA 3D printing.

In the first phase, we printed microchannel mold design using a 3D printer with XY resolution of 51 μm. Later to improve the dimensional accuracy and surface finish, we switched to a higher-resolution printer with XY resolution of 19 × 24 μm. Additionally, we incorporated reservoirs at both the inlet and outlet of the channel to promote steady and uniform flow conditions at the entrance, minimizing entrance effects and aiding the development of fully developed flow. Once the mold was

successfully printed, we used it for softlithography to cast a PDMS microchannel. After curing, the PDMS replica was carefully peeled off and bonded to a glass slide forming a leak proof and fully functional microfluidic device. A detailed discussion on the fabrication of these microchannel is provided in Chapter 4, Section 4.3.

After successfully fabricating the microchannel, we have performed experimental validation to ensure the accuracy and reliability of computational methodology. For this, we carried out a series of tests at various flow rates using a KD Scientific syringe pump. The values of flow rate and Reynolds number (Re) corresponding to various bulk shear rates considered in our experiments are given in Table 3. We monitored the pressure drop across the microchannel using Keller digital pressure gauge. An image of experimental setup is shown in Figure 3.2 (b).

The pressure drop values obtained from these experiments were then compared with those values computed by the computational fluid dynamics simulations and analytical calculations. As seen from Figure 3.2 (a), we observed a close agreement between the data obtained from computational, analytical, and experimental runs. This confirms the validity of our computational methodology, establishes reliability for its use in further numerical studies.

Table 3: Details of inlet flow conditions, including bulk shear rates, corresponding inlet flow rates, and associated Reynolds number of the flow.

S. No.	Bulk shear rate $\bar{\gamma}_\beta$ (s^{-1})	Flow rate Q (ml/min)	Reynolds number (Re)
1	100	0.0020394	0.069622
2	500	0.010197	0.34811
3	1000	0.020394	0.69622
4	2500	0.050985	1.7406
5	5000	0.10197	3.4811
6	10000	0.20394	6.9622
7	15000	0.30591	10.443

8	20000	0.40788	13.924
9	25000	0.50985	17.406
10	30000	0.61182	20.887

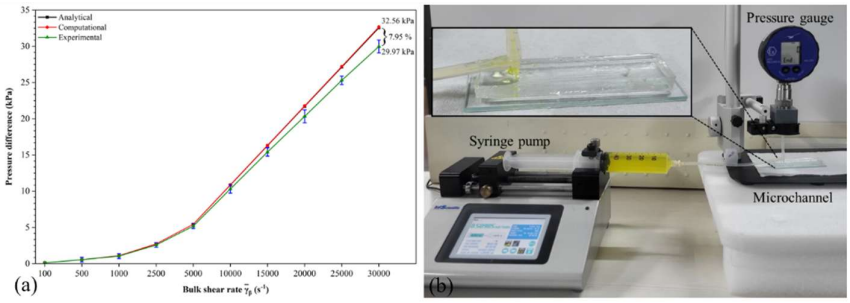

Figure 3.2: (a) Pressure differences analysis in a microchannel: analytical, computational, and experimental comparison. (b) Image of the experimental setup.

Chapter 4

Fabrication of Microchannel

The fabrication of microchannels plays a key role in the development of a microfluidic device, with precision in fabrication serving as a fundamental architecture for controlling and manipulating fluids at the microscale [73]. The early development of microfluidic devices happened with the advancement of the electronics industry. In the year 1947, physicists from Bell Labs, Walter. H. Brattain, John Bardeen, and William Shockley invented the transistor to fulfill the requirement of reliable mechanical relay systems [74]. Later in the year 1952, the US military was interested in exploring options to reduce the size of electronic circuits, such to make it capable of fitting inside proximity fuses. Jay W. Lathrop and Jim R. Nall were tasked to find possible ways, inspired by the application of photoresist, and they created the miniaturized hybrid integrated circuit (IC) with the transistor. In the year 1958, during the IRE Professional Group on Electron Devices (PGED) conference, they presented their first paper describing the process of transistor fabrication using a photographic technique named "photolithography" [74]. Photolithography later contributed to the development of the first IC prototypes and microchips. Later, researchers began to implement these techniques, exploring problems in molecular analysis, biodefence, molecular biology, etc. Stephen C. Terry in 1979 presented the study of a miniaturized gas chromatograph created on a silicon wafer, reducing the size of conventional equipment to one-third [75]. As the year passes, various projects contributed to progress in the field of microfluidics. One such project is the Human Genome Project, where scientists studied nucleic acids, creating devices that could handle tiny samples [76]. In 1986, Charles W. Hull introduced stereolithography, the process that creates 3D objects from ultraviolet light focused on photocurable polymer. In the same period, various microfluidic structures such as micropumps and microvalves were created using silicon micromachining [73]. Soft lithography, introduced

in the 1990s by George M. Whitesides and his research group at Harvard University, created a major shift in microfabrication. Through the use of elastomeric polymers such as PDMS, the replication of microfeatures from the mold became simple, yet provided high-quality patterns and structures. However, this method still requires the initial mold to be fabricated through cleanroom-based techniques, such as SU-8 photolithography. This maintains a reliance on traditional infrastructure [72, 76]. In recent years, with the advancement of technology in multiple areas, microfluidics fabrication has embraced digital manufacturing approaches as scalable, rapid, and cost-effective alternatives to traditional methods. Technologies using micro cutting, laser machining, and 3D printing are the prime focus in this digital manufacturing approach. These technologies allow for the fabrication of complex microchannel geometries with minimal infrastructure. The current trend in microfluidic research, including our work, aims to streamline the fabrication process by reducing the need for a cleanroom and improving rapid prototyping, which are critical factors for academic and translational research [77, 78].

In this chapter, we provided a comprehensive overview of various aspects of microchannel fabrication. First, we provided a brief review of the various materials used in microchannel fabrication, highlighting their suitability for different applications. This is followed by a discussion of different fabrication techniques, from conventional photolithography to digital manufacturing methods. Finally, we explored the low-cost fabrication methods used in our work for the fabrication of microfluidic devices.

4.1 Commonly used materials for microchannel fabrication

The choice of materials plays an important role in the design, functionality, and manufacturing of microfluidics devices. At the microscale, properties such as optical clarity, chemical resistance, and biocompatibility are more amplified. Over the years, various kinds of material have been used to accommodate these properties [80].

4.1.1 Silicon

In the early stages of the microfluidics platform development, silicon was among the first material of choice. This is due to its availability, chemical compatibility, thermal stability, and its established use in semiconductor industries [81]. However, several limitations such as optical transparency, brittleness, and high cost of microfabrication were not in favour of silicon. This prompted researchers to explore alternate materials suited for broader microfluidic applications [82].

4.1.2 Glass

Following silicon, glass was preferred as an alternative in microfluidic device fabrication due to its superior optical transparency, chemical inertness, and thermal stability. These properties made the glass well suited for applications involving fluorescence imaging, high temperature chemical reactions, and biocompatibility [82]. Glass also offers excellent compatibility with surface modification techniques. Despite these advantages, the microchannel fabrication in glass typically requires harsh etchants (e.g., hydrofluoric acid) and high-temperature bonding, which increases the cost of production and imposes highly regulated safety and equipment requirements. The brittle nature of glass also limits its use in flexible microfluidic systems [79, 80]. As a result, it lacked in its adoption in mass-produced or low-cost platforms in comparison with polymers and hybrid materials.

4.1.3 Polymers

The limitations of rigid, inorganic substrates have led to the widespread adoption of polymers, which now dominate microfluidic device fabrication. This is due to their low cost, ease of processing, and flexibility in designing devices from nanoparticle synthesis to fluid manipulation. They also provide good optical transparency and bonding compatibility with the glass surface, thus making them ideal for creating microfluidic platforms with enhanced performance and versatility [80].

PDMS has become one of the most widely used elastomers in the field of microfluidics. This is due to its biocompatibility, optical transparency, low autofluorescence, gas permeability, and compatibility with soft lithography techniques. PDMS is particularly valued for biological compatibility, such as biochemical assays, ease of cell culture, sorting and patterning of cells/ proteins, and various applications, including Lab-on-a-Chip (LoC) platforms [83]. However, PDMS presents challenges such as pH-dependent molecules absorption, water evaporation through the matrix, and deformation under mechanical stress or high temperatures. Some of these properties act as barriers to its effective use in organic synthesis processes. These limitations have led to the exploration of alternative polymeric materials depending on the specific properties and targeted applications [81].

Thermoplastics such as Polymethyl methacrylate (PMMA) [84], Polycarbonate (PC) [80], and Cyclic olefin copolymers/polymers (COC/COP) [85] have become popular choices in microfluidics due to their excellent mechanical properties, optical transparency, and compatibility with high-throughput fabrication techniques like injection molding and hot embossing.

Epoxy resins, such as SU-8, bisphenol-based formulations, etc., are widely used for producing high-aspect-ratio microstructures and durable master molds. SU-8 is a negative photoresist, is structured using ultraviolet (UV) photolithography, and is known for its strong chemical resistance, mechanical robustness, and good adhesion to substrates [78]. It plays a crucial role in soft lithography processes, particularly when working with PDMS. However, once cured, SU-8 becomes highly inert, making it difficult to remove or modify, and it can be prone to cracking or delamination under mechanical stress. Despite these limitations, epoxy resins are still widely used for the fabrication of high-resolution microscale features.

Hydrogels are water-rich, porous, 3D polymerized networks that support the diffusion of small molecules and biological particles. Their

biocompatibility, biodegradability, and extracellular matrix (ECM) like structure make them ideal for 3D cell culture, drug delivery, and biosensing. They promote cell adhesion and growth, mimicking natural tissue environments [81]. However, due to their mechanical weakness, they are rarely used as the main material in microfluidic devices. Instead, they are integrated into microfluidic devices as membranes, or functional layers [86].

The diverse range of fabrication materials discussed above can be compared based on their properties and fabrication compatibility for the development of microfluidic systems as summarized in Table 4 below.

Table 4: Overview of common materials used in microfluidic device fabrication.

Material	Type	Properties	Compatible fabrication methods
Silicon	Inorganic	High thermal stability, chemical stability	Photolithography, Etching [78]
Glass	Inorganic	Optical clarity, chemical resistance, biocompatibility, thermal stability	Etching, Laser machining [86, 87]
PDMS	Elastomer polymer	Biocompatibility, optical transparency, gas permeability, flexibility	Soft lithography [89]

PMMA	Thermoplastic polymer	Rigidity, transparency, solvent resistance, mechanical strength	Hot embossing, Laser machining [90]
COC/COP	Thermoplastic polymer	Chemical resistance, low water absorption, high optical transparency	Injection molding, Hot embossing [89, 90]
SU-8	Epoxy polymer	High-aspect-ratio patterning, chemical stability, rigidity	Photolithography [80]
Hydrogels	Hydrophilic polymer	Biocompatibility, permeability, biodegradability	3D printing [92]

4.2 Fabrication techniques for microfluidic devices

Fabrication of microfluidic devices requires precise methods to build features such as microchannels, pillars, valves, etc., that control fluid flow. Since these devices can be made from different materials such as glass, polymers, or hydrogels, each material needs a specific fabrication approach depending on its properties and end-use application. Low fabrication cost is another essential factor, as most microfluidic devices are designed for single use. Over the years, various fabrication technologies have evolved from traditional cleanroom-dependent processes to more accessible digital manufacturing approaches. Each method has its own advantages in terms of resolution, throughput, design flexibility, and compatibility with various materials [93].

4.2.1 Photolithography

Photolithography is a foundational microfabrication process that uses light to transfer patterns from a photomask to a photoresist, typically applied on a silicon or glass substrate. This technique offers sub-micron resolution and is widely used for creating master molds or direct patterns. At first, a thin layer of photoresist is spin-coated onto a clean silicon or glass substrate. The coated surface is then exposed to UV light through a photomask on which the desired pattern is defined. Depending on the type of photoresist, positive or negative, these exposed areas become either soluble or insoluble. After development, the unprotected regions of the substrate are subjected to etching. This process creates precisely patterned microstructures, which can be directly used as master molds for further device fabrication [93].

4.2.2 Soft lithography

Soft lithography is a widely used technique for replicating microstructures, often used with photolithography. It is preferred for its cost-effectiveness, ease of replication with various materials. The process begins by creating a negative master mold using photolithography. To replicate these features, a PDMS prepolymer is mixed with a cross-linking agent, degassed to remove air bubbles, and poured onto the mold [77]. The setup is then cured at elevated temperatures (preferably at 60-70 ºC) to solidify the elastomer. Once cured, the PDMS replica is peeled off and processed further, resulting in a flexible and functional microfluidic device.

4.2.3 Etching

Etching is a subtractive microfabrication process used to selectively remove material from a substrate. It begins with applying an etch-resistant mask, followed by the removal of exposed areas using either wet or dry etching methods. Wet etching involves chemical solutions like potassium hydroxide (KOH), sodium hydroxide (NaOH), or hydrofluoric acid (HF), which dissolve unmasked material through

chemical reactions [93, 94]. Whereas dry etching uses plasma or ionized gases such as oxygen (O_2), carbon tetrafluoride (CF_4), or sulfur hexafluoride (SF_6) to etch the surface [96]. Reactive ion etching (RIE) is a combination of both wet and dry etching and is widely used for its anisotropic etching nature. RIE helps in high-resolution pattern transfer with vertical sidewalls. These techniques are the essential part of forming high-aspect-ratio microchannels and complex structures in microfluidic devices, particularly for silicon, glass substrates [97].

4.2.4 Hot embossing and injection molding

Hot embossing is a replication-based technique used to fabricate microchannels in thermoplastic substrates. It involves heating the polymer material until soft, then pressing a master mold into it under high pressure and temperature. Once cooled and solidified, the patterned structure is released from the mold, resulting in precise microchannels. The process is cost-effective and offers high reproducibility, making it suitable for prototyping and batch production [97, 98].

Injection molding is another high-throughput manufacturing process ideal for large-scale production. It involves clamping pre-fabricated mold halves, followed by injection of molten polymer, cooling of parts within the mold, and then ejection of the final product. Process parameters such as pressure, temperature, and cooling time are finely tuned for optimal results. This fabrication process has enabled the mass fabrication of complex, miniaturized devices with quality and dimensional accuracy [99, 100].

4.2.5 Laser machining

Laser machining is a fabrication technique that enables rapid and flexible patterning of microchannels on a wide range of materials. Though lasers can be costly, they are often accessible and cost-effective in maintenance. The process relies on laser-induced thermal degradation, where short, high-energy pulses break chemical bonds, causing localized material ejection. This technique avoids the use of

hazardous chemicals and supports direct writing without masks. However, limitations include variation in feature quality, reproducibility, and surface irregularities [101, 102].

4.2.6 3D printing

3D printing is gaining popularity in microfabrication, offering the ability to build complex, multilayered microfluidic structures that are difficult to achieve using conventional methods like photolithography or etching. It is an additive manufacturing process that builds devices layer by layer from digital models such as computer-aided designs (CAD). This enables rapid prototyping and design flexibility. The system comprises a 3D printer, specialized print materials, and software to control layer deposition across X, Y, and Z axes. Among the popular techniques, stereolithography (SLA) stands out for microfluidics due to its high resolution, smooth surface finish, and dimensional control. It uses a UV light source to cure photosensitive resins. This capability makes SLA suitable for fabricating microchannel devices for biomedical and analytical applications in cost cost-effective manner [103, 104].

4.3 Fabrication approach used in the present work

In this work, we have explored low-cost rapid manufacturing techniques aimed at simplifying the microfluidic device fabrication process. At first, we used laser machining to fabricate the microchannel on silica glass slide and PDMS block. Later, to improve the precision, resolution, and design flexibility, we adopted SLA based 3D printing. These methods enabled rapid and cost-effective fabrication of microfluidic devices.

4.3.1 Microchannel fabrication using CO_2 laser

Initially, the microchannels were fabricated using a carbon dioxide (CO_2) laser, which operates at the wavelength of 10.6 μm. This type of laser is effective for silica-based glass substrates, as it absorbs infrared radiation at this wavelength, enabling material ablation without

requiring complex etching processes. During the laser machining, we regulated specific process parameters to influence the shape of machined microchannels, this includes the repetition rate (rep rate) which defines how frequently laser pulses are emitted, the duty cycle which influences the energy applied per unit time, the focal length or standoff distance (SOD) which affects beam focus and spot size, and the travel speed which determines how quickly the laser moves over the surface.

We performed laser machining on silica-based microscopic glass slides, which were positioned at a fixed focal distance of 11.5 cm. During the first trial, we used a repetition rate of 10 Hz, at 60% duty cycle, and maintained the SOD of 11.5 cm while varying the travel speed to study its effect on the dimensions of machined microchannel. Details of these parameters are listed in Table 5. To evaluate the machined features, we conducted microscopic characterization, and the results are shown in Figure 4.1. It can be observed from Figure 4.1 that as travel speed increased from 60 mm/min to 110 mm/min, it resulted in a reduction in the width of machined microchannels, decreasing from approximately 0.868 mm to 0.800 mm.

Table 5: Process parameters of CO_2 laser machining on glass with varying travel speed.

Figure	Rep rate (Hz)	Duty cycle (%)	SOD (cm)	Speed (mm/min)
a	10	60	11.5	60
b	10	60	11.5	70
c	10	60	11.5	80
d	10	60	11.5	90
e	10	60	11.5	100
f	10	60	11.5	110

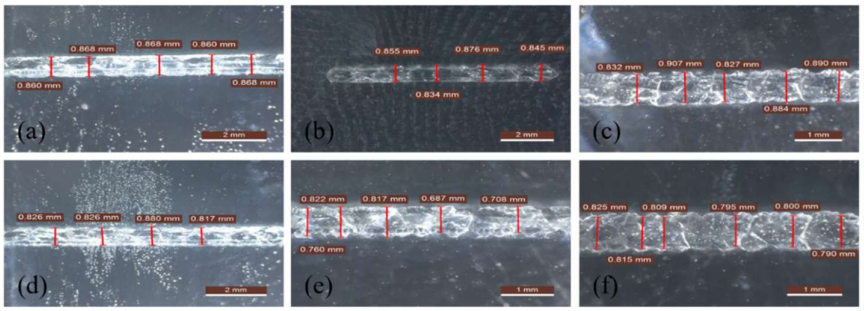

Figure 4.1: Optical characterization of laser-machined microchannels on glass surface under different travel speeds: (a) 60 mm/min, (b) 70 mm/min, (c) 80 mm/min, (d) 90 mm/min, (e) 100 mm/min, and (f) 110 mm/min.

This trend can be due to the reduced interaction time between the laser beam and the substrate at higher speed, which limits the amount of energy delivered per unit length and results in narrower ablation paths. However, during the visual inspection of the machined channels, we observed irregular and uneven edges along the sidewalls. This irregularity is likely due to the brittle nature of glass, which is prone to microcracking and uncontrolled fracturing when subjected to localized thermal stress from high-energy laser pulses. To address this issue, we deposited a thin sacrificial layer of aluminium (Al) onto the surface of the glass slide prior to machining. This can absorb and redistribute some of the laser energy, thus reducing thermal stress at the glass surface, and it also minimizes crack propagation, resulting in smoother and more uniform channel edges. In this second set of experiments, we varied the duty cycle from 20% to 60%, while keeping other parameters constant. With this, we can analyze the effect of energy delivered on the quality of the machined features. The complete set of process parameters is given in Table 6, and the optical characterization of the resulting microchannels under different duty cycles is presented in Figure 4.2. The results presented in Figure 4.2 show that increasing the duty cycle from 20% to 60% led to a gradual increase in the width of the machined microchannels, ranging from ~0.710 mm to ~0.784 mm. This occurs

because a higher duty cycle increases the thermal energy transferred to the substrate, which enlarges the ablation area.

Table 6: Process parameters of CO_2 laser machining on glass with varying duty cycle.

Figure	Rep rate (Hz)	Duty cycle (%)	SOD (cm)	Speed (mm/min)
a	10	20	11.5	80
b	10	40	11.5	80
c	10	60	11.5	80

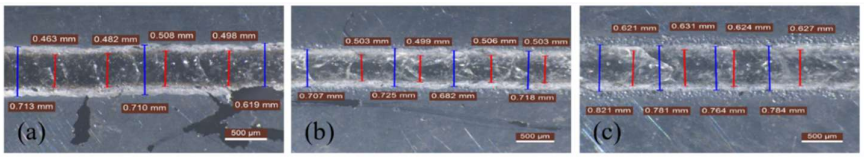

Figure 4.2: Optical characterization of laser-machined microchannels on glass surface under different duty cycles: (a) 20 %, (b) 40 %, and (c) 60 %.

Figure 4.3 shows a comparison between uncoated and Al-coated glass slides, highlighting that channels formed on the coated surface were slightly narrower. This is due to the sacrificial aluminium layer, which absorbs and dissipates part of the laser energy, reducing direct thermal stress on the brittle glass, which limits the extent of material removal. We also observed that the surface quality of channels on Al-coated glass slide was improved, exhibiting fewer microcracks and smoother edges compared to the uncoated glass slide. However, despite improved edges, visual inspection revealed that the surface finish of the laser machined glass microchannels remains unsuitable for biological applications involving blood flow, such as vascular stenosis studies. The presence of abrupt surface irregularities can cause local disturbances in shear stress, which may trigger unwanted platelet activation and clot formation. Additionally, we also observed that the laser-machined glass slides became more fragile, with an increased tendency to crack or shatter

during handling and transportation. This mechanical instability makes them less suitable for developing reliable and durable microfluidic devices, especially in applications requiring repeated handling or integration with external components. Due to the challenges encountered during laser micromachining of glass, such as edge irregularities, surface cracks, and increased fragility post-fabrication, we next performed CO_2 laser machining on cured PDMS blocks, a soft, elastomeric material widely used in microfluidics for its optical clarity, flexibility, and biocompatibility.

Similar to glass, an inverse relationship between travel speed and channel size was observed where higher travel speeds resulted in narrower channels, as can be seen from Figure 4.4. However, during PDMS machining, we noticed laser-induced pyrolysis. This was evident from dark residues near the edges as seen from Figure 4.4 (a, b). Such deposits may interfere with biological compatibility, as they could chemically react with biomolecules introduced into the channel. Process parameters used for machining PDMS are given in Table 7.

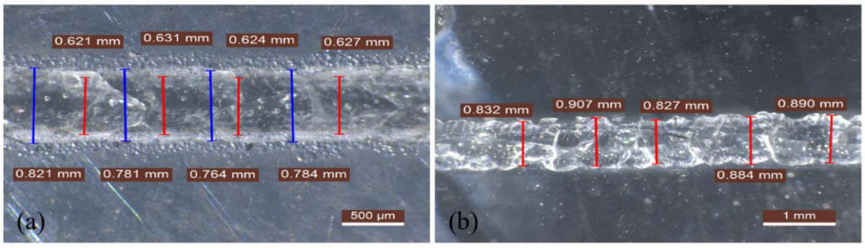

Figure 4.3: Comparison of machining on aluminium (a) coated and (b) uncoated glass side.

Additionally, when we machined more complex geometries such as T-shaped (Figure 4.4 (c)) microchannel junctions, we observed dimensional irregularities around the intersection regions, which make these fabricated PDMS microchannels unsuitable for bifurcation studies, where precise geometrical accuracy and smooth transitions are essential.

Table 7: Process parameters of CO_2 laser machining on PDMS block with varying speed.

Figure	Rep rate (Hz)	Duty cycle (%)	SOD (cm)	Speed (mm/min)
a	10	60	11.5	60
b	10	60	11.5	100

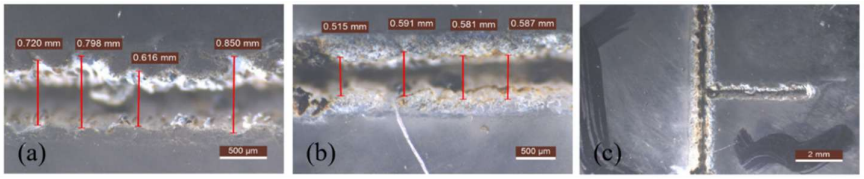

Figure 4.4: Optical characterization of laser machined microchannels on PDMS block. (a, b) Channels fabricated by varying travel speed while keeping repetition rate, duty cycle, and stand-off distance constant. (c) Machining of T shaped microchannel junction.

As we explored CO_2 laser machining on both silica-based glass slides and cured PDMS slabs. The resulting microchannels exhibited significant limitations, including poor surface finish, dimensional irregularities, material damage such as microcracks, and pyrolysis residues. Additionally, laser machining posed challenges in creating variable-width channels and complex geometries, such as T-shaped junctions. These shortcomings make laser-fabricated microchannels less suitable for experimental studies involving vascular stenosis, where smooth, precise channel geometries are critical. To overcome these fabrication challenges and achieve higher resolution, better surface quality, and more consistent channel profiles, we shifted our focus to 3D printing based on vat photopolymerization systems.

4.3.2 Microchannel fabrication using SLA 3D printing

Initially, we used a Creality LD-002H 2K LCD 3D printer with an XY resolution of 51 μm to print straight and serpentine microchannel patterns, as shown in Figure 4.5 (a, d). This geometry was modelled using Autodesk Fusion 360. The digital model was then exported in stereolithography (.stl) format to a slicing software (Chitubox) for generating the 3D printable file. We printed these molds on Kapton polyimide sheets, both with (Figure 4.5 (a)) and without raft support (Figure 4.5 (d)). In this setup, we studied the effect of the base layer exposure time, which affects the adhesion between the printed part and the build plate, as well as evaluating the influence of raft support on dimensional stability, print adhesion, and overall surface flatness of thin, detailed microchannels. From Figure 4.5 (b, c, e, f), we can see that both printed channel dimensions were approximately 5-7 times larger than the original design dimensions. However, molds printed without raft support exhibited greater dimensional variation and minor warping compared to those printed with raft support. We also observed that the mold printed directly on Kapton polyimide without raft support was not suitable for soft lithography, as it underwent distortion during detachment from the build plate after printing. This behavior limited their mechanical integrity and usability as master molds, suggesting that raft structures help to stabilize the initial layers and reduce distortion during the post-printing process.

Despite these dimensional discrepancies, we observed that the printed molds showed visually smooth surface finishes, or resin residue. This proof-of-concept demonstrated that even with a mid-range 3D printer and standard resin, the process could yield reliable mold features. However, as we have used clear resin in this trial, it posed challenges during optical characterization, such as the transparency-limited edge definition under the microscope. Additionally, the printed channels showed limited accuracy in reproducing fine dimensions, and curved geometries lacked smooth surface profiles, making them less suitable

for applications requiring precise and complex microchannel paths. To improve these dimensional inaccuracies and surface quality, we proceeded with a better resolution SLA printer, the Phrozen Mighty 12K, with XY of 19 × 24 µm. Using this setup, we fabricated straight microchannels of 200 × 100 µm cross-sections and 36.5 mm in length. At the layer exposure of 2.2 s, the required microchannel dimensions were obtained. Upon optical inspection (as shown in Figure 4.6 (a)) of the fabricated microchannel, we observed significantly improved dimensional accuracy and smoother surface finish compared to previous attempts. These observations demonstrate that enhanced resolution has helped us in replicating fine microchannel features.

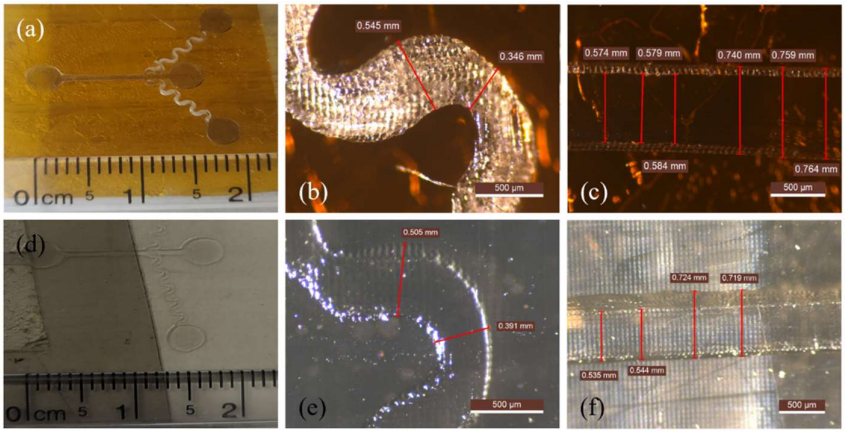

Figure 4.5: 3D printing and characterization of microchannel molds. (a-c) Mold printed directly on Kapton polyamide sheet (without raft support) and corresponding characterization of serpentine and straight channels. (d-f) Molds printed with raft support and corresponding characterization of serpentine and straight channels.

Later, we used this mold as a master template for the soft lithography process. A curable elastomer of PDMS was poured onto the mold along with its curing agent in the ratio of 10:1. We then degassed the mixture to remove any trapped air bubbles and subsequently cured it in an oven at 65°C for 2 hours to solidify. Once cured, the elastomer has the negative imprint of the 3D printed microchannel. We carefully peeled this cured PDMS from the mold and examined its dimension under a

microscope, as shown in Figure 4.6 (b). The replicated microchannel structure was then prepared for bonding to a flat glass substrate. To achieve this, we spin-coated a thin layer of PDMS along with its curing agent (5:1) onto a clean glass slide to ensure uniform thickness. This coated slide was then partially cured by placing it in an oven for a specific pre-curing time of 20 minutes at 65°C.

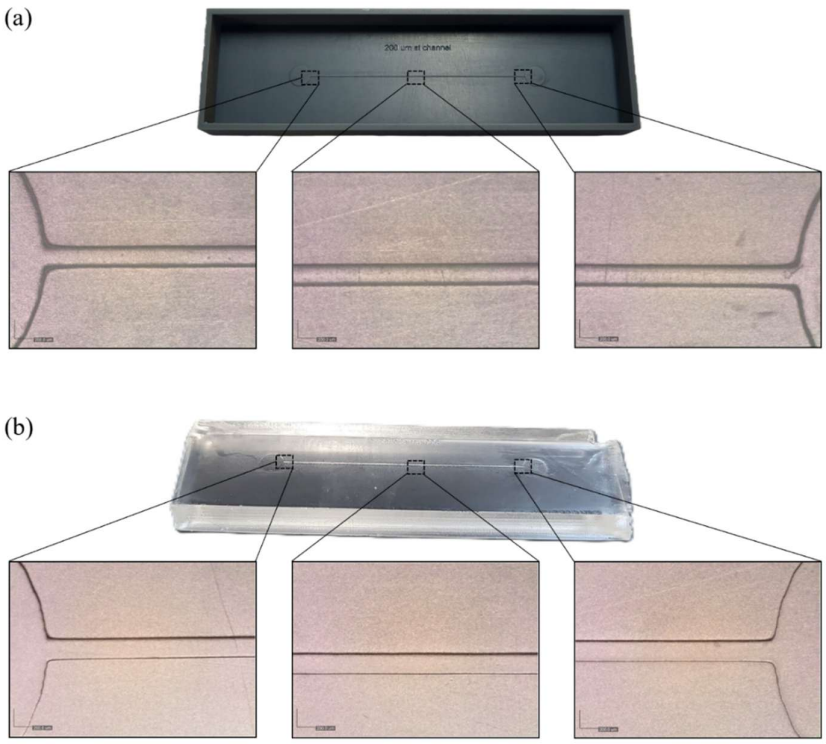

Figure 4.6: Microscopic characterization of (a) 3D printed mold and (b) PDMS replica showing well-defined microfluidic channel.

Once the coating reached a partially cured state, the replicated PDMS microchannel was then gently pressed on the coated glass slide to initiate bonding. This assembly was then returned to the oven for a final curing cycle (50 minutes at 65°C), which completed the bonding process, resulting in a sealed microfluid device. The entire microchannel fabrication process is illustrated in Figure 4.7. This method helps in building a strong adhesion between the microchannel and the glass slide, creating a leak-proof, optically transparent device. We later used this

fabricated microfluidic platform for the experimental validation of the computational methodology, as discussed earlier in Chapter 3, Section 3.2.

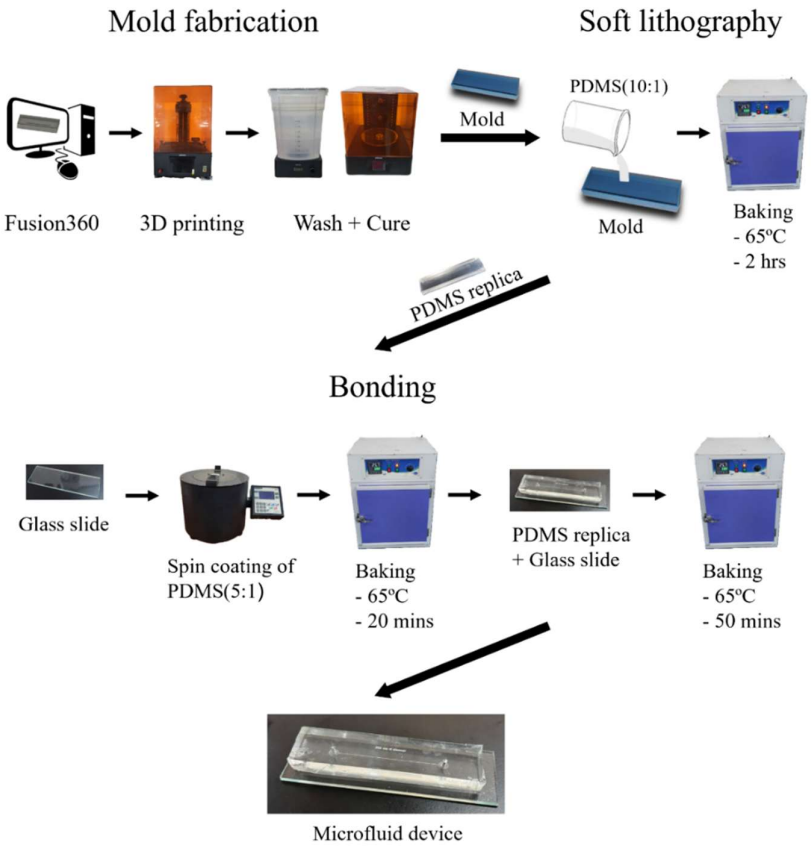

Figure 4.7: Fabrication process of microfluid device: showcasing mold fabrication, soft lithography-based replication, and device bonding.

Chapter 5

Study of Hemodynamic Changes Resulting from Variations in Stenosis Geometry

5.1 Geometrical model

In this work, we have explored the hemodynamic effects of microvascular narrowing using a set of idealized stenosed geometries. These variations allowed us to examine the effect of different stenosis shapes on local flow dynamics, and their effects on platelet activation, aggregation, and further thrombus formation.

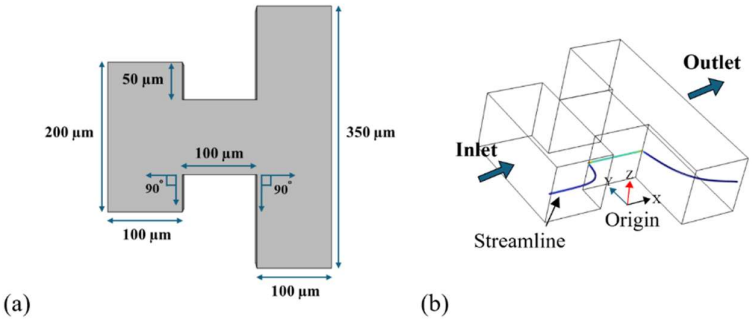

Figure 5.1: (a) Schematic of converging diverging geometry representing microvascular stenosis, with key dimensions labelled. The channel height Z_0 is 100 µm. (b) 3D view of CFD simulation showing inlet and outlet flow.

In the present study, we employed a converging-diverging section to mimic the localized narrowing. The following parameters were varied across different models:

Bulk shear rate ($\overline{\gamma}_{\beta}$): Flow conditions were simulated over a range of bulk shear rates (100 s^{-1} to 30,000 s^{-1}), capturing both low and high shear environments relevant to microcirculation. Details of which are briefed in Table 3 of Chapter 3.

Degree of stenosis (width variation): The stenosed throat width was varied from 25 µm to 100 µm, representing different levels of luminal blockage.

Contraction and expansion angles: The transition angles at pre- and post-stenosed regions were adjusted between 30° and 90°, allowing investigation of flow patterns.

Curvature of the throat: The curvature of the stenotic region was modified from radius of 0 µm to 50 µm to study how sharp versus smooth transitions influence recirculation zones and shear distributions.

Figure 5.1 presents the dimensions of geometry used in this study. By systematically modifying specific geometrical parameters, the study aims to uncover how subtle changes in stenosed architecture can influence blood flow dynamics and provide insights into thrombosis formation.

5.2 Grid independence study

A grid independence study was carried out to ensure that the results are not affected by the number of mesh elements used. This step is important to make sure that the simulation outcomes remain accurate, even if the mesh size is changed. We used a convergence criterion of residuals less than 10^{-6} to confirm the stability of the solution. The boundary conditions used in the simulations are explained in chapter 3, section 3.1.

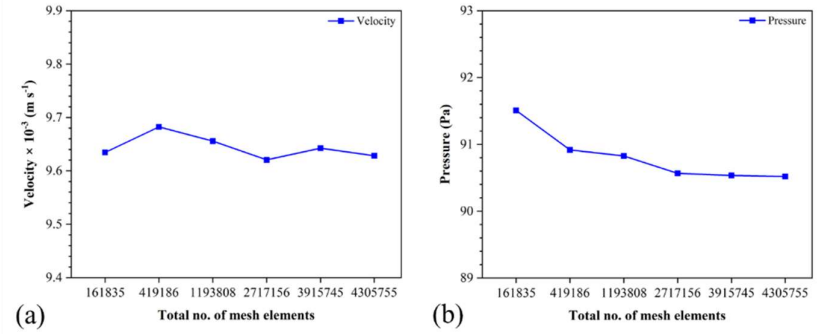

Figure 5.2: Grid independence analysis showing (a) velocity and (b) pressure variations with different mesh elements, evaluated at a point located 1 µm above the stenosed wall.

To test grid independence, we observed velocity and pressure at a fixed point located 1 micron above the wall of the stenosed region (as shown

in Figure 5.2). Several mesh densities were tested, and six key cases are discussed as given in Table 8. Results from Figure 5.2 showed that Mesh 5 showed consistent values of velocity and pressure, while also keeping the simulation time reasonable. As a result, we chose Mesh 5 as the final mesh setup and used its configurations for all further simulations.

Table 8: Mesh refinement parameters for grid independence study of stenosed geometry.

Mesh type	Number of elements in the entire mesh	No. of degrees of freedom solved
Mesh 1	161835	149013
Mesh 2	419186	356249
Mesh 3	1193808	973661
Mesh 4	2717156	3711213
Mesh 5	**3915745**	**4688093**
Mesh 6	4305755	5508793

5.3 Results and Discussions

5.3.1 Effect of bulk shear rate ($\overline{\gamma}_{\beta}$) on hemodynamic parameters in microvascular stenosis

We performed a series of numerical simulations across a range of inlet bulk shear rates (as listed in Table 3) to investigate their influence on blood flow behavior. The analysis focused on the streamline passing 1 μm above the stenosed region. This region has been chosen as an area of interest because platelet margination is more likely to occur in small blood vessels; this unique flow characteristic favours the movement of platelets towards the vessel wall. From Figure 5.3, we can observe a sharp increase in shear rate at both the entrance and exit of the stenosed region, corresponding to positions near -50 μm and 50μm, respectively. At lower bulk shear rates (100 s^{-1} to 2,500 s^{-1}), the difference between these peak values remains modest. However, as the bulk shear rate increases (ranging from 5,000 s^{-1} to 30,000 s^{-1}), the difference between

these peaks becomes more prominent, as shown in Figure 5.3(a, b). Notably, at a bulk shear rate of 30,000 s^{-1}, the peak shear rate near the -50 µm location is nearly 2.5 times higher than the corresponding peak near 50 µm. This localized increase in shear rate at the onset of the stenosis is particularly significant in the context of platelet dynamics. Platelets are known to be highly responsive to variations in shear stress [106].

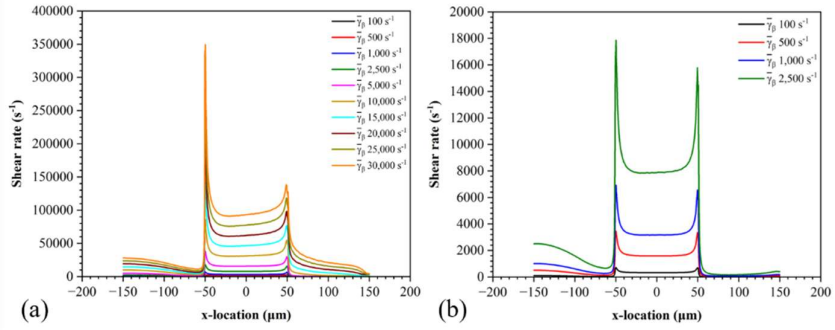

Figure 5.3: Variation of shear rate along the streamline near the wall of the stenosed microvascular geometry. (a) Comparison across bulk shear rates $\bar{\gamma}_\beta$ = 100 - 30,000 s^{-1}. (b) Magnified view for $\bar{\gamma}_\beta$ = 100 - 2,500 s^{-1}.

Exposure to elevated shear can lead to initiating intracellular signalling pathways associated with their activation. High shear conditions enhance the unfolding of vWF, which facilitates binding to platelet receptors, which is an early step in platelet adhesion [32]. Consequently, the sharp increase in shear stress at the entrance of the stenosis may act as a trigger for platelet activation, increasing the likelihood of adhesion to the vessel wall or to already adherent platelets. Furthermore, as platelets continue to traverse through the stenosed region, they are subjected to sustained elevated shear rates. Prolonged exposure to such conditions can increase activation signals and promote aggregation. This sustained mechanical stimulus, coupled with the disturbed flow patterns within the stenosis, may significantly enhance the prothrombotic potential of the microvascular environment. Figure 5.4 shows the velocity distribution as blood flows through a stenosed microvessel, where each subplot provides an insight into how velocity varies across

the domain. The streamline distribution in Figure 5.4 shows the regions of flow recirculation.

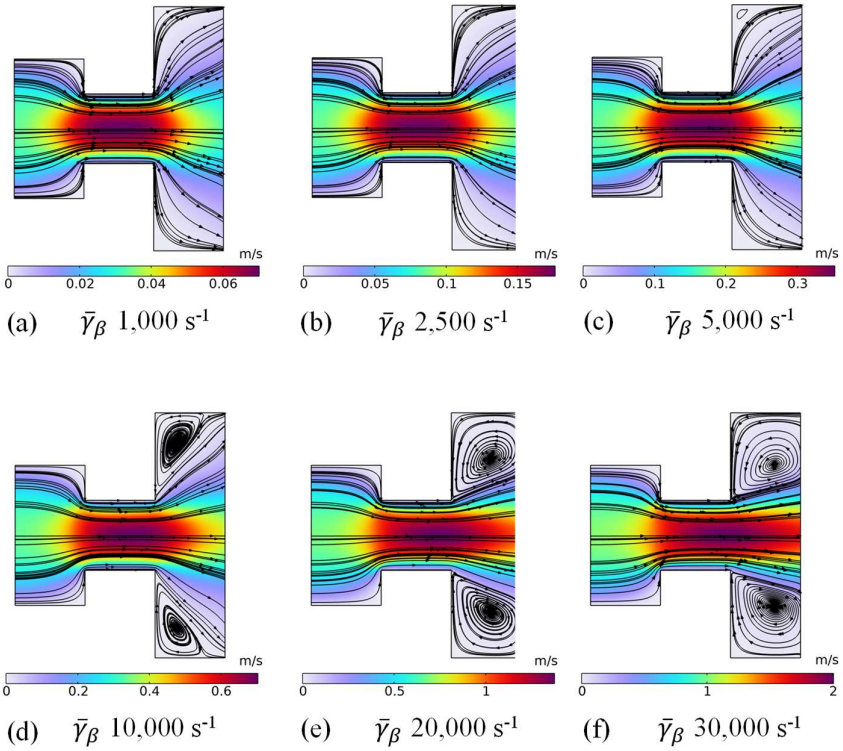

Figure 5.4: Velocity field distribution for different bulk shear rates on a plane passing from Z = 50 µm from base. (a) $\bar{\gamma}_\beta$ 1,000 s^{-1}, (b) $\bar{\gamma}_\beta$ 2,500 s^{-1}, (c) $\bar{\gamma}_\beta$ 5,000 s^{-1}, (d) $\bar{\gamma}_\beta$ 10,000 s^{-1}, (e) $\bar{\gamma}_\beta$ 20,000 s^{-1}, (f) $\bar{\gamma}_\beta$ 30,000 s^{-1}.

In all cases, as the flow enters the stenosed region, it undergoes noticeable acceleration. This is visually represented by the shift in colour gradients from green in the wider upstream sections to red within the constricted area, indicating elevated velocity magnitudes. In the downstream of the stenosis, flow separation leads to the formation of recirculation zones, indicated by vortices in the flow profile. As the bulk shear rate increases, these recirculation zones become more prominent and well defined. At lower shear rates (Figure 5.4 (a-c)), recirculation zones are small and relatively weak. However, for the bulk shear rate of 10,000 s^{-1} and above, these zones expand significantly and become more intense, particularly near the edges of the post-stenosed area as seen in

Figure 5.4 (d-f). Platelets near the vessel walls are prone to becoming trapped in recirculation zones, where low or reverse flow facilitates their activation and aggregation. For high bulk shear rates, the risk of thrombus formation is not limited to the stenosed region itself but also extends to the post-stenosed region, where activated platelets may accumulate. This increases the possibility of thrombus growth beyond the stenosis, potentially obstructing the flow downstream.

5.3.2 Hemodynamic effects of varying stenosis width in microvascular flow

Narrowing of blood vessels due to stenosis is a critical geometric factor. As stenosis progresses over time, the degree of narrowing increases, making it essential to understand constriction's effects on local hemodynamics and platelet behavior. To evaluate this, we studied the effect of width variation in stenosed region on flow behavior and hemodynamic parameters. Results indicate that as the stenosed region narrows, the average shear rate increases drastically, as shown in Figure 5.5 (a). Specifically, a reduction in stenosis width from 100 μm to 75 μm led to a 1.5 to 2-fold rise in shear rate across varying bulk shear conditions. Further narrowing to 50 μm and 25 μm amplifies this effect, producing roughly 3.5-fold and 12-fold increases respectively (as shown in Figure 5.5 (b-d)). This exponential rise in shear rate reflects the increasing mechanical stress that blood cells, particularly platelets, are subjected to within the constricted vessel segment.

Progressive narrowing not only raises the local shear but also increases the likelihood of flow separation and vortex formation. We can see from Figure 5.6, when the stenosis width is reduced to 25 μm, pronounced recirculation zones form even at lower bulk shear rates ($\bar{\gamma}_{\beta} \sim 5{,}000\ s^{-1}$). These zones are significantly less developed in wider stenosed geometries, such as in width of 100 μm under the same conditions. The presence of these recirculation regions creates disturbed flow areas characterized by low or reverse velocities and longer residence times for blood cells. Platelets circulating near the vessel wall are especially

affected by these disturbed flow conditions, as high shear rates, particularly in the entrance and throat of the stenosis, are known to trigger platelet activation. Additionally, in the post-stenotic region, platelets trapped in recirculation zones are exposed to prolonged shear and flow disturbances, further enhancing their likelihood of becoming activated. These activated platelets may begin to aggregate and adhere to the endothelial surface or to each other, initiating early thrombus formation. Therefore, as stenosis progresses, it not only changes the way blood flows but also creates conditions that strongly favour blood clot formation.

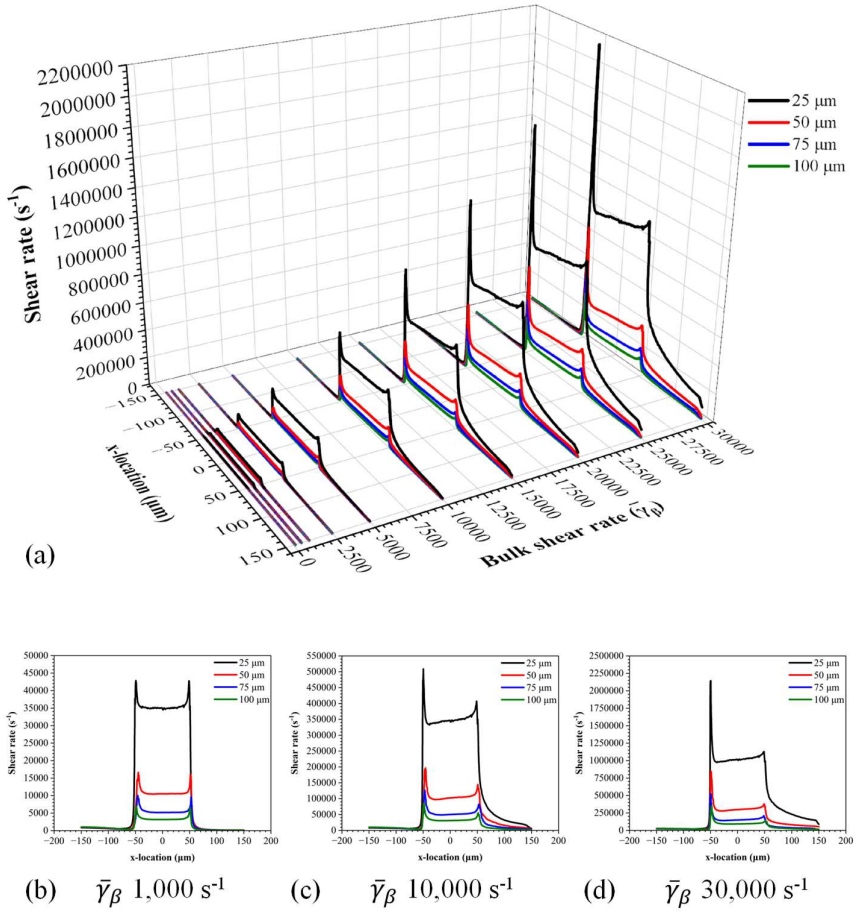

Figure 5.5: Effect of stenosis width (25 - 100 μm) on shear rate along a streamline near the microchannel wall. (a) Variation across bulk shear rates $\bar{\gamma}_\beta$ = 100 - 30,000 s^{-1}. (b-d) Profiles at $\bar{\gamma}_\beta$ = 1,000, 10,000, and 30,000 s^{-1}.

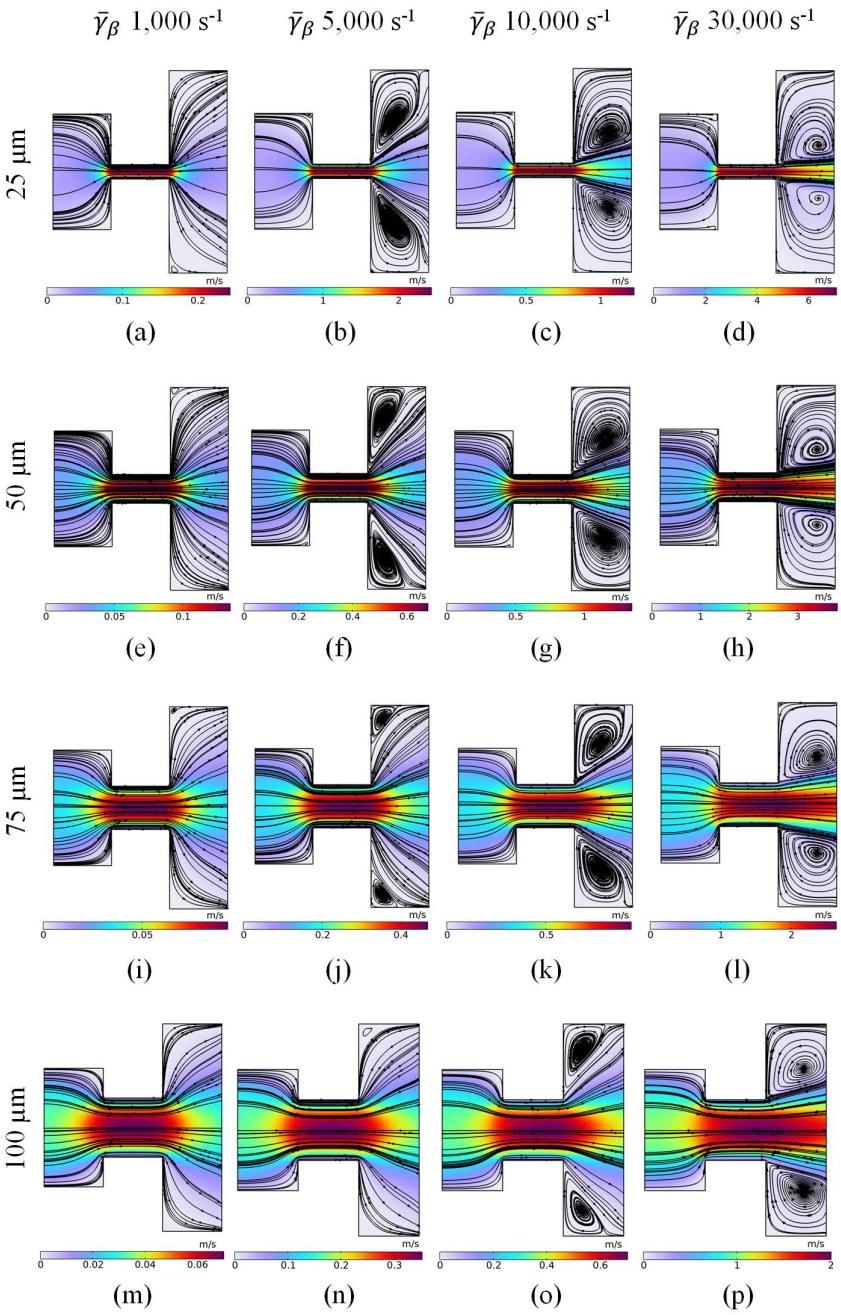

Figure 5.6: Effect of stenosis width variation (25 µm, 50 µm, 75 µm, and 100 µm) on the velocity field at varying bulk shear rates (i.e. $\bar{\gamma}_\beta$ 1,000 s^{-1}, $\bar{\gamma}_\beta$ 5,000 s^{-1}, $\bar{\gamma}_\beta$ 10,000 s^{-1}, $\bar{\gamma}_\beta$ 30,000 s^{-1}).

Narrowing increases the magnitude of mechanical stimuli experienced by platelets and introduces complex flow features that favour platelet accumulation. Over time, this can escalate into significant thrombus formation, potentially leading to partial or complete blockage of the

vessel. In the context of microvascular systems, such blockages can severely affect downstream flow, affecting endothelial health.

5.3.3 Influence of angular topology of stenosed microvessels on hemodynamic behavior

The angular topology of a stenosed vessel is defined by the inlet and outlet angles of the constriction. It plays a crucial role in shaping local flow dynamics and environment experienced by circulating blood components.

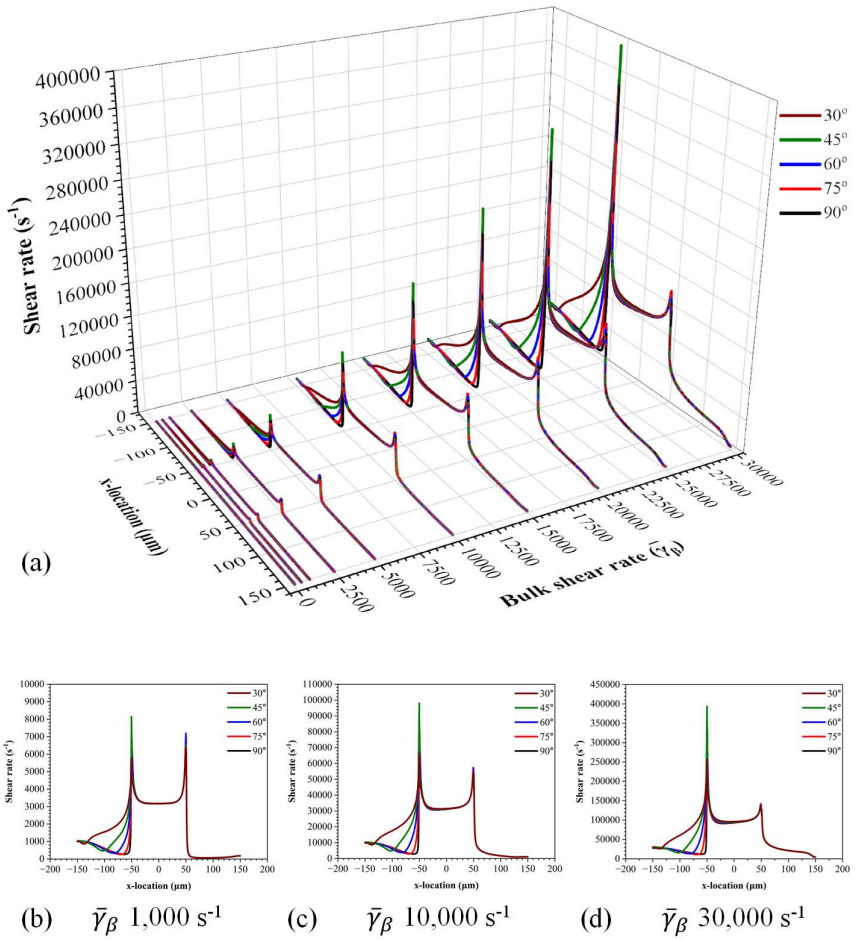

Figure 5.7: Effect of inlet angles (30º - 90º) on shear rate along a streamline near the microchannel wall. (a) Variation across bulk shear rates $\bar{\gamma}_\beta$ = 100 - 30,000 s^{-1}. (b-d) Profiles at $\bar{\gamma}_\beta$ = 1,000, 10,000, and 30,000 s^{-1}.

In microvascular systems, where the geometry is highly confined and flow is sensitive to small structural changes, angular variations can significantly affect shear distribution, streamline behavior, and vortex formation. These factors, in turn, influence how platelets respond to mechanical stimuli, particularly in regions prone to disturbed flow and high shear gradients. Over time, stenotic geometries may evolve not only in severity but also in their angular profiles due to irregular plaque deposition. Therefore, understanding the effect of angular variation on hemodynamics is essential to assess platelet activation mechanisms and the risk of thrombosis in complex microvascular stenoses.

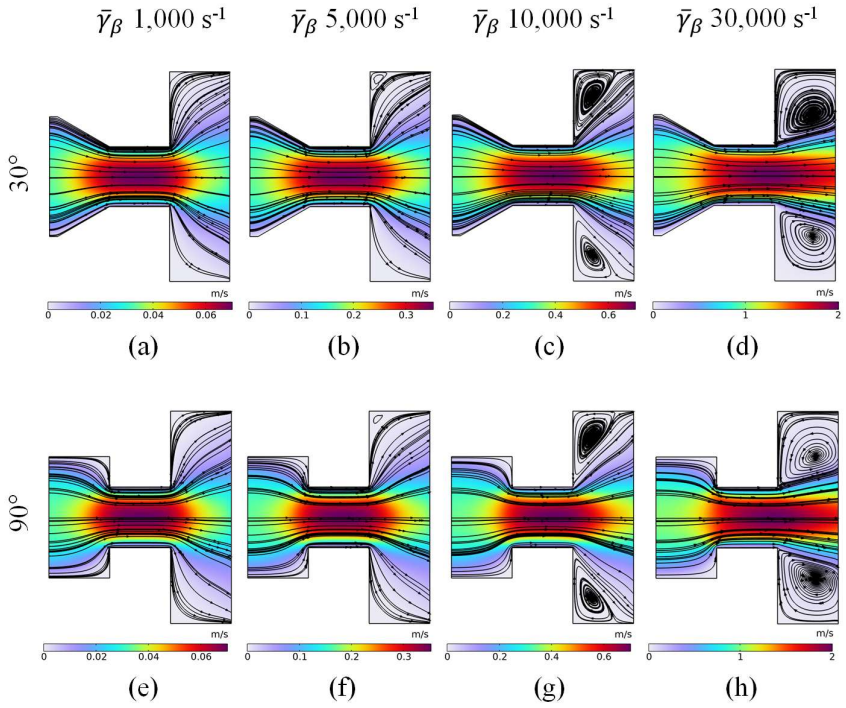

Figure 5.8: Influence of inlet angle geometry (30º and 90º) on the velocity distribution across various bulk shear rates (i.e. $\bar{\gamma}_\beta$ 1,000 s^{-1}, $\bar{\gamma}_\beta$ 5,000 s^{-1}, $\bar{\gamma}_\beta$ 10,000 s^{-1}, $\bar{\gamma}_\beta$ 30,000 s^{-1}).

To investigate the influence of angular topology on the flow field and hemodynamic behavior in the stenosed microvascular region, we carried out simulations across various inlet and exit angles at multiple bulk shear rates. From Figure 5.7, we can see that the inlet angle plays a

significant role in shaping the local shear rate distribution. Specifically, as the inlet angle decreases from 90º to 30º, a general trend of reduced peak shear rates is observed at the entrance of the stenosed region (~ -50 µm). This trend remains consistent across all evaluated bulk shear rates. Interestingly, at an inlet angle of 45º, a localized increase in peak shear rate is observed, deviating from the otherwise consistent reduction seen with 60° and 30° angles, as shown in Figure 5.7 (b-d).

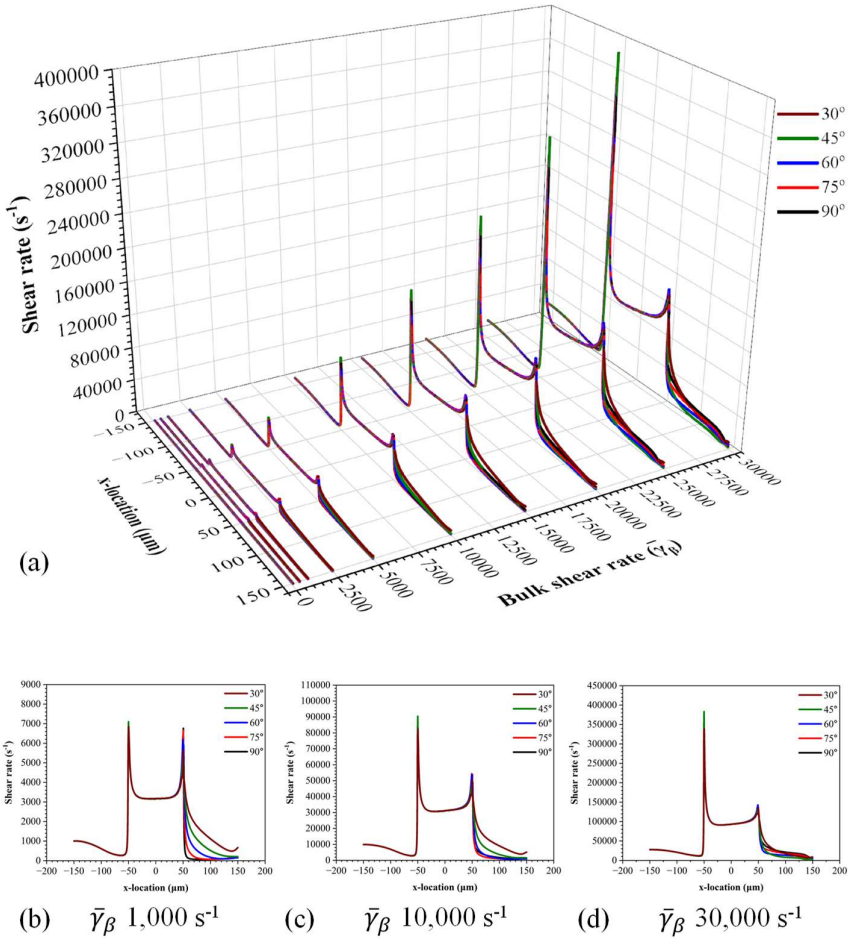

Figure 5.9: Effect of exit angle (30º - 90º) on shear rate along a streamline near the microchannel wall. (a) Variation across bulk shear rates $\bar{\gamma}_\beta$ = 100 - 30,000 s^{-1}. (b-d) Profiles at $\bar{\gamma}_\beta$ = 1,000, 10,000, and 30,000 s^{-1}.

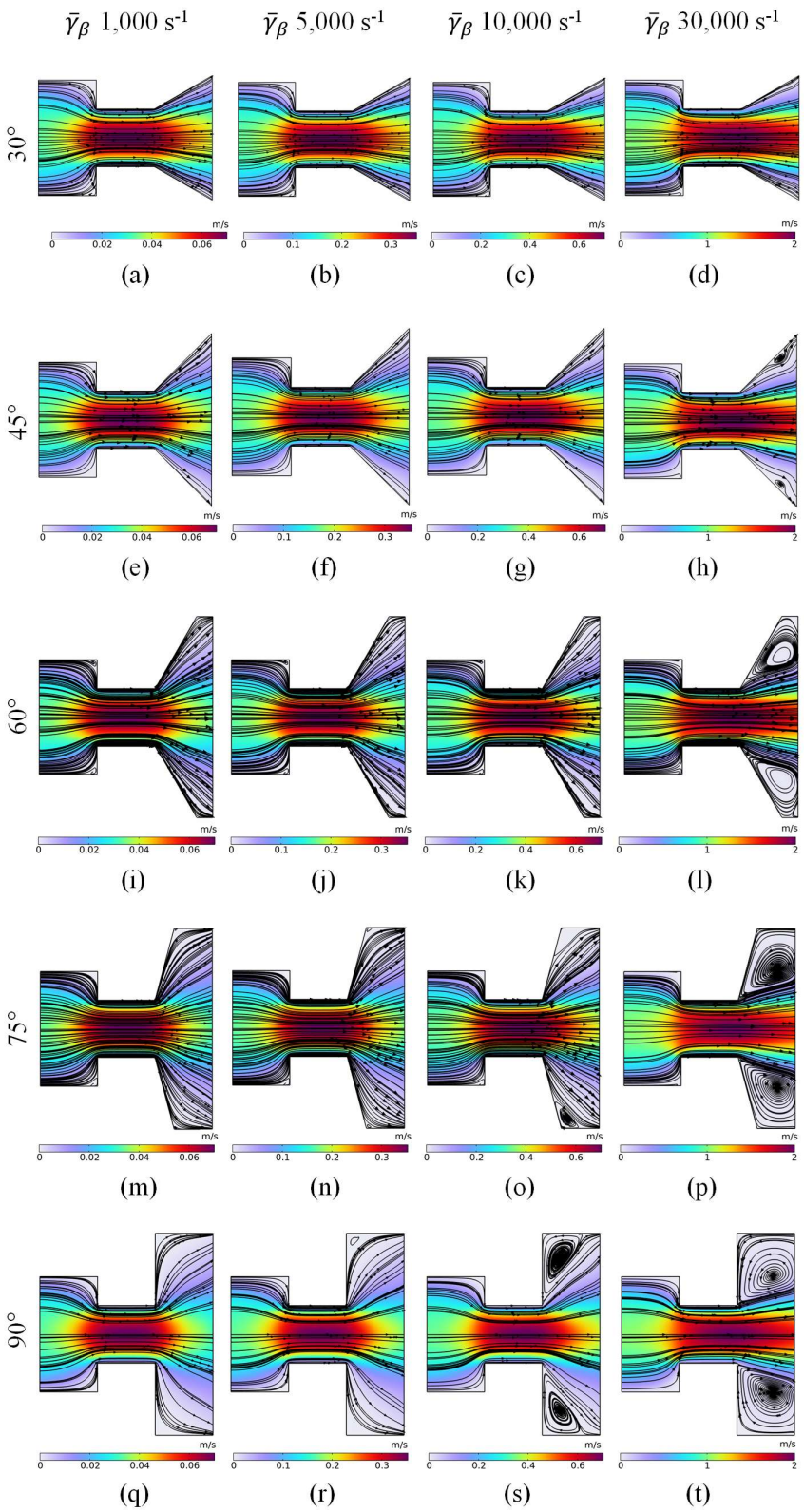

Figure 5.10: Velocity flow field variation for varying exit angle (30º,

45º, 60º, 75º, and 90º) at different bulk shear rates (i.e. $\bar{\gamma}_\beta$ 1,000 s^{-1}, $\bar{\gamma}_\beta$ 5,000 s^{-1}, $\bar{\gamma}_\beta$ 10,000 s^{-1}, $\bar{\gamma}_\beta$ 30,000 s^{-1}).

As the flow progresses through the stenosed region, shear rates rapidly decline and stabilize, maintaining a relatively high local shear rate within the constriction. However, inlet angle variation does not significantly affect the average shear rate within the stenosed zone. As the flow reaches downstream of stenosed region, the inlet angle variation has minimal influence on the formation of recirculation zones, as shown in the velocity distribution from Figure 5.8. This trend holds true across all inlet bulk shear rates, suggesting that inlet angle alone does not substantially alter flow separation or vortex generation in the post-stenotic regions. In contrast, the exit angle of the stenosed region appears to have a more direct impact on downstream flow stability. As the exit angle decreases from 90º to 30º, we observed a noticeable reduction in the tendency for vortex formation, regardless of the applied bulk shear rate, as shown in the velocity distribution in Figure 5.10.

Narrower exit angles promote smoother flow reattachment and reduce the likelihood of flow reversal, which helps in reducing the recirculation zones. This minimizes platelet residence time in disturbed flow zones. This can be beneficial in reducing the risk of platelet accumulation and subsequent thrombus formation. Figure 5.9 shows that despite these changes in flow structure, the overall shear rate distribution along the flow path remains largely unchanged. From Figure 5.9 (b-d), it can be seen that only a slight decrease in peak shear rate is noted at the outlet as the exit angle is reduced. This suggests that while the flow becomes more stable, key factors influencing platelet activation such as high shear gradients are not significantly altered. Therefore, platelet movement and adhesion in such geometries are likely governed more by global flow dynamics and cell-to-cell or cell-to-wall interactions than by localized shear rate variations alone.

5.3.4 Role of radial curvature in shaping hemodynamics within microvascular stenosis

In stenotic vessels, the curvature of the throat region determines how abruptly or gradually blood flows through the narrowed section. Variations in this curvature directly influence key hemodynamic parameters such as shear rate distribution, vortex formation, and the formation of recirculation zones, all of which are closely linked to platelet motion, activation, and aggregation.

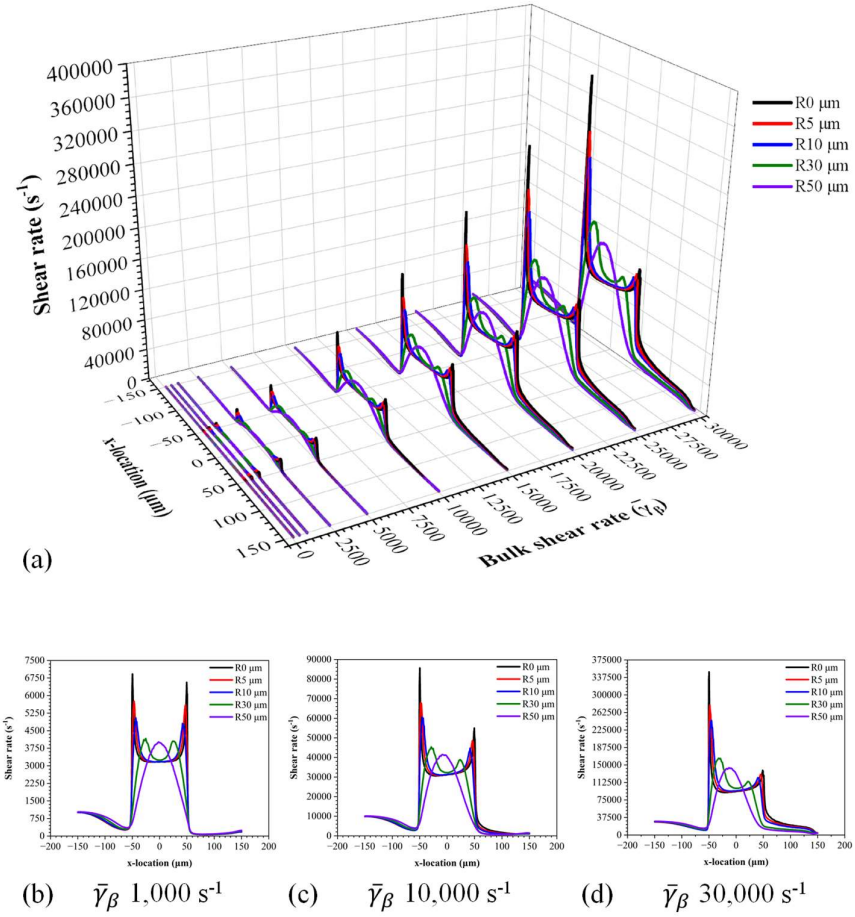

Figure 5.11: Effect of curvature radius (0 - 50 μm) on shear rate along a streamline near the microchannel wall. (a) Variation across bulk shear rates $\bar{\gamma}_\beta$ = 100 - 30,000 s^{-1}. (b-d) Profiles at $\bar{\gamma}_\beta$ = 1,000, 10,000, and 30,000 s^{-1}.

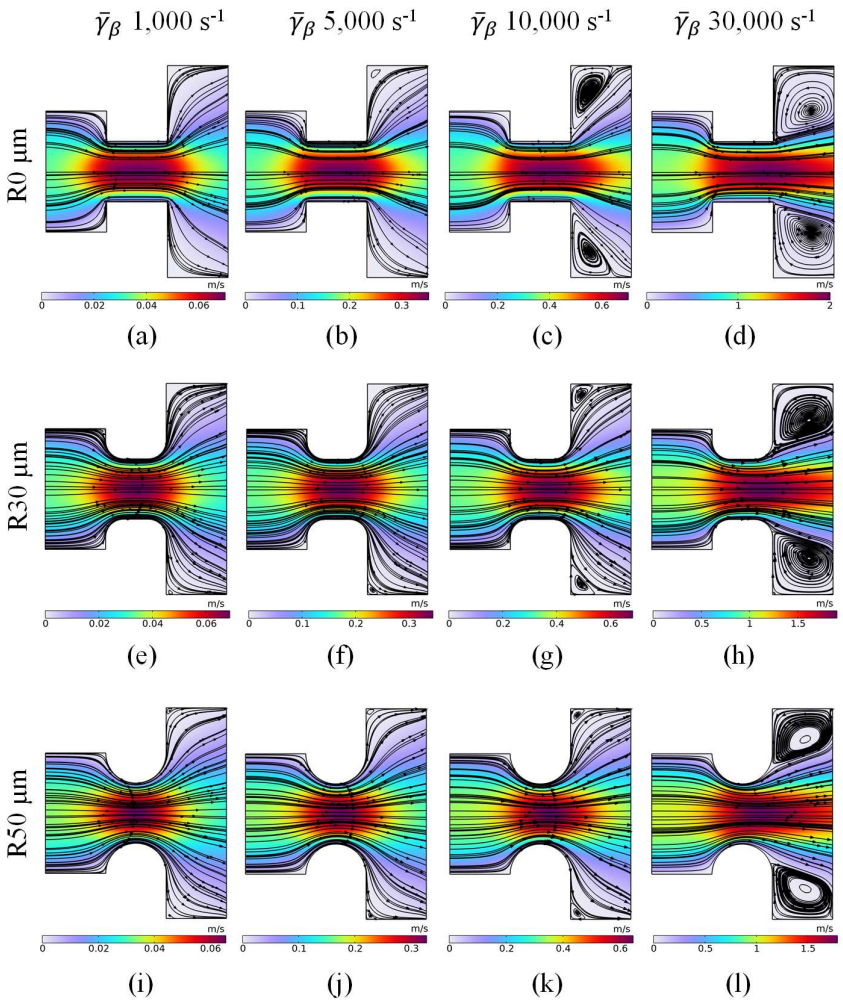

Figure 5.12: Velocity distribution showing the effect of radial curvature (0 µm, 30 µm, 50µm) on flow dynamics of stenosed microvessel at various bulk shear rates (i.e. $\bar{\gamma}_\beta$ 1,000 s^{-1}, $\bar{\gamma}_\beta$ 5,000 s^{-1}, $\bar{\gamma}_\beta$ 10,000 s^{-1}, $\bar{\gamma}_\beta$ 30,000 s^{-1}).

As illustrated in Figure 5.11, increasing the radius of curvature from 0 µm (R0 µm) to 50 µm (R50 µm) results in a substantial reduction in peak shear rate at the throat of the stenosis. A sharper (R0 µm) curvature introduces higher shear gradients, while a smoother (R50 µm) curvature facilitates a more gradual shear distribution. Figure 5.11 (b-d) shows that this transition leads to a more uniform shear stress distribution, minimizing localized spikes. Furthermore, as shear gradients reduce

with increasing curvature, the risk of sustained platelet stimulation decreases. This reduction in continuous mechanical loading reduces the likelihood of vWF-mediated platelet adhesion and aggregation. Moreover, from Figure 5.12, we can see that an increase in radial curvature correlates with a shift in recirculation zones present in the downstream of the stenosed region. This trend is observed consistently across a wide range of bulk shear rates. The overall velocity field and downstream flow behavior play critical roles in influencing platelet transport and residence time. As the curvature radius increases, the flow through the stenosed region becomes smoother. Post stenotic zones are typically characterized by low or reverse velocity and are known to trap platelets near the vessel wall. In sharply curved stenoses, flow separation occurs more easily, resulting in large and persistent vortices downstream. These disturbed flow regions prolong platelet residence time near the endothelium, thereby increasing the probability of platelet interactions that can initiate clot formation. A smoother curvature (R50 μm) reduces flow separation and shifts the recirculation zones towards the vessel wall, thus minimizing areas of low shear and stagnation, as shown in Figure 5.12.

This may reduce the contact duration of platelets with the vessel wall and decrease the chances of localized aggregation. Together, the modifications in the shear and velocity field due to changes in radial curvature directly impact platelet behavior. Increased shear at the throat can serve as a primary activator of platelets, while recirculation zones downstream provide the environment for platelet accumulation and aggregation, which creates the favourable environment for clot formation. The radial curvature of microvascular stenosis has a profound effect on local hemodynamics and the resulting biological response of platelets. A larger curvature radius leads to reduced shear gradients and more uniform stress distributions. Understanding and optimizing these geometrical parameters are essential in both computational modelling and clinical device design aimed at mitigating thrombotic risk in microvascular systems.

5.4 Conclusion

This study comprehensively examines the effect of variations in both flow conditions and geometric features of microvascular stenosis on the hemodynamic environment, with a particular emphasis on understanding flow features that influence platelet activation and thrombus formation. The results highlight that changes in bulk shear rate have a sound influence on the local hemodynamic behavior. As the bulk shear rate increases, the velocity through the stenosed region rises sharply. This results in elevated shear stresses, especially at the entrance and exit of the constriction. These regions experience steep shear gradients, which are known to act as potent mechanical triggers for platelet activation. Moreover, higher bulk shear also increases the strength and extent of downstream recirculation zones, where platelets may remain trapped for longer durations, further enhancing their potential for aggregation and thrombus formation.

In addition to flow rate, the width of the stenosed region is another critical factor shaping the local flow dynamics. As the width reduces, both the magnitude of shear and the size of recirculation zones increase. These disturbed regions not only prolong platelet residence time near the vessel walls but also generate a mechanical microenvironment that favours their activation, adhesion, and downstream accumulation. The angular geometry of the stenosed section further regulates flow behavior. Inlet angles influence how sharply the flow accelerates into the stenosed region, with steeper angles (90º) producing higher local shear peaks. Interestingly, intermediate angles showed nonlinear behavior. Meanwhile, the exit angle plays a more dominant role in regulating downstream flow behavior. Smaller (30º) exit angles reduce the tendency for vortex formation and recirculation, potentially reducing the entrapment of activated platelets. Lastly, the radial curvature of the stenosis throat influences both shear profiles and downstream recirculation. A sharp curvature (R0 μm) results in abrupt changes in flow direction, high shear distribution, and large recirculation zones. In contrast, increasing the radius of curvature to more gradual profiles (R50

μm) smoothed out shear gradients and shifted vortex formation towards the vessel wall. The reduction in both shear distributions and recirculation zones contributed to a hemodynamic environment less conducive to platelet activation and thrombus initiation. These benefits were consistent across a range of shear rates, demonstrating the effect of curvature on hemodynamics of stenosed microvessels.

Overall, the findings from this study establish that both flow rate and geometrical configuration significantly alter the mechanical cues within a stenosed microvessel. Elevated bulk shear, narrow constrictions, steady angular transitions, and sharp curvature all amplify platelet-relevant shear fields and disturbed flow patterns, which are known for pro-thrombotic environments. Whereas, smooth geometric transitions, wider throats, gradual inlet and outlet angles, and increased curvature reduce pathological flow behavior and thrombogenic potential. These insights have direct implications for vascular biology research, such as cardiovascular disease modelling, and the design improvement of blood-wettable medical devices such as stents, vascular grafts, and microfluidic platforms. By carefully regulating these parameters, it is possible to replicate pathological flow conditions, offering new ways for the study of thrombosis at the microscale.

Chapter 6

Hemodynamic Analysis of Single, Multiple Stenoses and Post-Stenotic Dilatation Microvessels

6.1 Geometrical model

In this study, we have considered various geometrical configurations representing different conditions of microvascular narrowing, including a healthy vessel with no obstruction, vessels with a single stenosis, vessels with multiple stenosis, especially double and triple stenosis, and advanced configurations where each stenosis (single, double, and triple) is followed by a PSD region. PSD is the region of vessel widening that typically occurs downstream of a stenosed region. This widening occurs due to increased pressure, formation of recirculation zones, abnormal shear stress, etc., resulting from disturbance caused by the stenosed region, which can lead to weakening and remodelling of vessel wall.

The dimensions of various stenosed sections in microvessels with or without PSD conditions are shown in Figure 6.1. For all models, the total axial length of microvessel (X_0) is 4.6 mm, while the depth (Z_0) was kept uniform at 100 μm. In geometries involving multiple stenosis, the narrowed regions were placed at uniform intervals of 1 mm along the axial length of the vessel. This range of configurations enables a comprehensive assessment of how different stenosis patterns influence blood flow dynamics at the micro level and promote formation of mural thrombosis.

6.2 Grid independence study

To ensure accuracy and reliability of computational results, a grid independence analysis has been carried out. This has been done to confirm that the results are not influenced by mesh resolution. A standard residual criterion of 10^{-6} was implemented to ensure

convergence and numerical stability during iterations. The boundary conditions applied in the computational simulations are detailed in section 3.1 of chapter 3. Here, to evaluate grid independence, we monitored the velocity and pressure at a location 2 μm above the vessel wall of the stenosed region. This region was chosen because it reflects the flow conditions experienced by platelets travelling near the vessel wall, where hemodynamic forces significantly affect their behavior.

Multiple mesh densities were examined for two distinct configurations: (i) a microvessel with single stenosis, and (ii) a single stenosed microvessel with PSD region. Out of total configurations tested, five representative cases are given in Table 9.

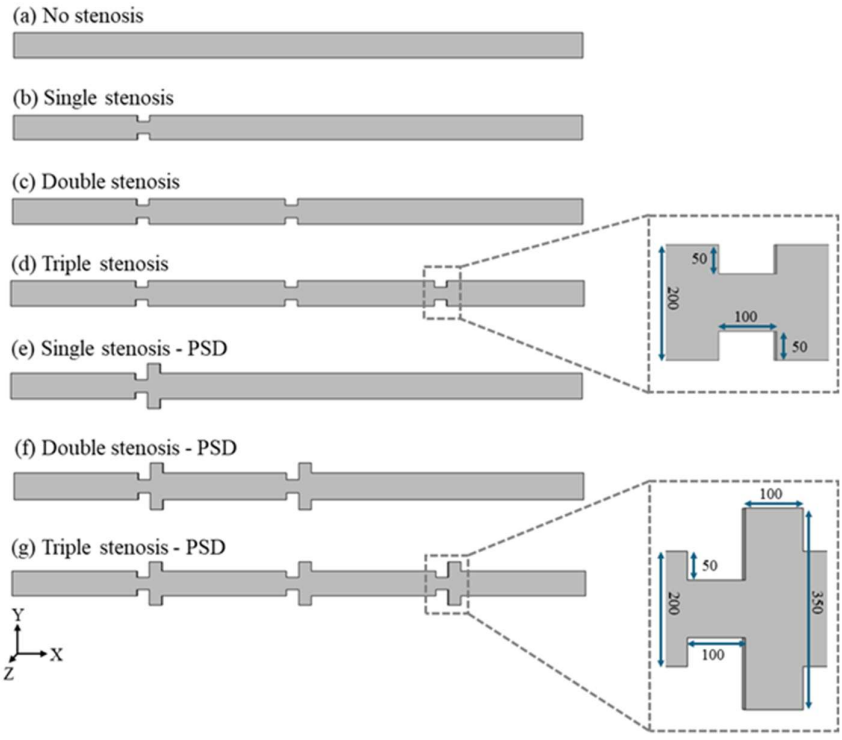

Figure 6.1: Schematic representation of microvessels showing (a) healthy vessel without stenosis, vessel with (b) single stenosis, (c) double stenosis, (d) triple stenosis, (e) single stenosis followed by PSD, (f) double stenosis with PSD, and (g) triple stenosis with PSD. All dimensions are given in micrometers (μm).

Table 9: Mesh refinement parameters for grid independence study of single stenosis and single stenosis with PSD geometry.

Mesh type	Number of elements in the entire mesh (Single stenosis)	Number of elements in the entire mesh (Single stenosis with PSD)
Mesh 1	263975	284494
Mesh 2	439657	516854
Mesh 3	1207523	1376883
Mesh 4	**2977030**	**3161830**
Mesh 5	13199502	13933819

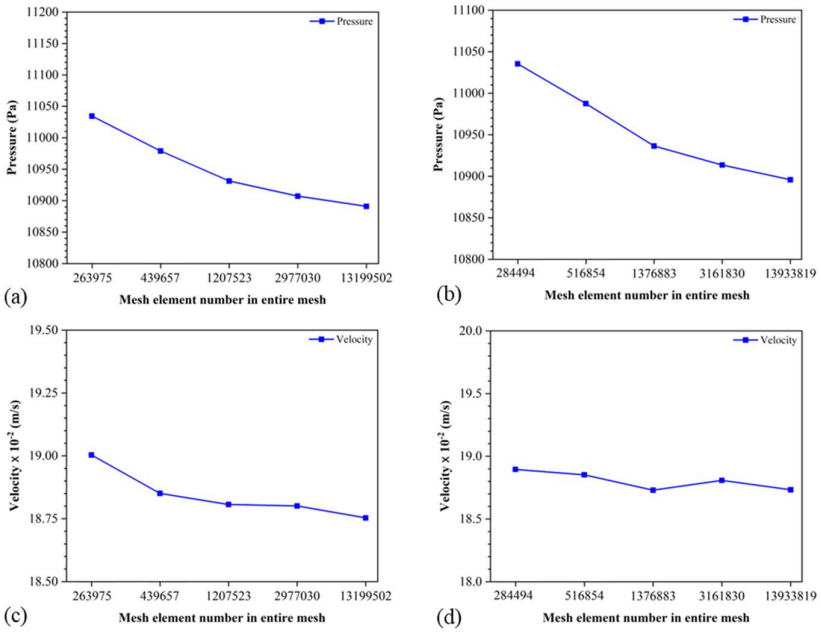

Figure 6.2: Grid independence analysis for pressure variation with varying numbers of mesh elements in (a) single stenosis, (b) single stenosis with PSD microvessel. Corresponding variation of velocity for (c) single stenosis and (d) single stenosis with PSD microvessel.

The results from Figure 6.2 show that Mesh 4 exhibits stable velocity and pressure magnitude, providing an optimal balance between accuracy and computational time for both cases. Therefore, we selected Mesh 4

as the optimal mesh configuration and used it for all subsequent simulations.

6.3 Results and Discussions

6.3.1 Analysis of velocity distribution in stenotic and post-stenotic dilatation (PSD) microvessels

A wide range of numerical simulations were carried out across different stenosed microvessel geometries, each subjected to various inlet bulk shear rates (as per Table 3), with a primary goal to closely examine flow patterns through the regions of vascular stenosis and post-stenotic dilatation. These geometrical features significantly alter flow characteristics. The velocity distribution from Figure 6.3(a) shows no change in core and surrounding streamlines as the flow passes through a healthy vessel, indicating a stable and uniform flow field. In contrast, as the blood passes through the stenosed microvessels with and without PSD, symmetrical recirculating zones can be observed as shown in Figure 6.3(b-d). These high-strength recirculation vortices form in the region immediately downstream of the stenosis, particularly in PSD zones, as can be seen in Figure 6.3(e-g). These recirculation zones indicate low velocity and reversed flow direction, which can increase residence time of platelets.

The narrowing of the vessel leads to a considerable rise in the flow velocity at the stenosis core, greatly exceeding the inlet flow, and indicating a strong acceleration through the constricted region. This rapid change in velocity over a small spatial region gives rise to a steep velocity gradient, particularly near the vessel walls. It is well-established in the literature that platelet activation is directly linked to elevated shear stresses [106]. Under pathological conditions, it acts as a mechanical stimulus which can initiate the activation, adhesion, and aggregation process. Elevated shear stresses are primarily associated with the high-velocity gradient, particularly in the transition region between the core and downstream recirculation zone of stenosis. Figure 6.3 represents the

quantitative velocity gradients across various stenosed geometries. The data includes velocity distribution for single and multiple stenosed microvessels at inlet bulk shear rate of only 500 s^{-1} and 30,000 s^{-1}. As platelets predominantly migrate near the vessel walls in microvessels, this region becomes critically important when studying factors that influence their physiological behavior. Therefore, to accurately capture the flow characteristics, a streamline passing 2 µm above the bottom wall has been considered to evaluate the velocity and stress effects. This approach allows for a more precise assessment of the mechanical cues that platelets are exposed to, which plays a key role in their activation and aggregation.

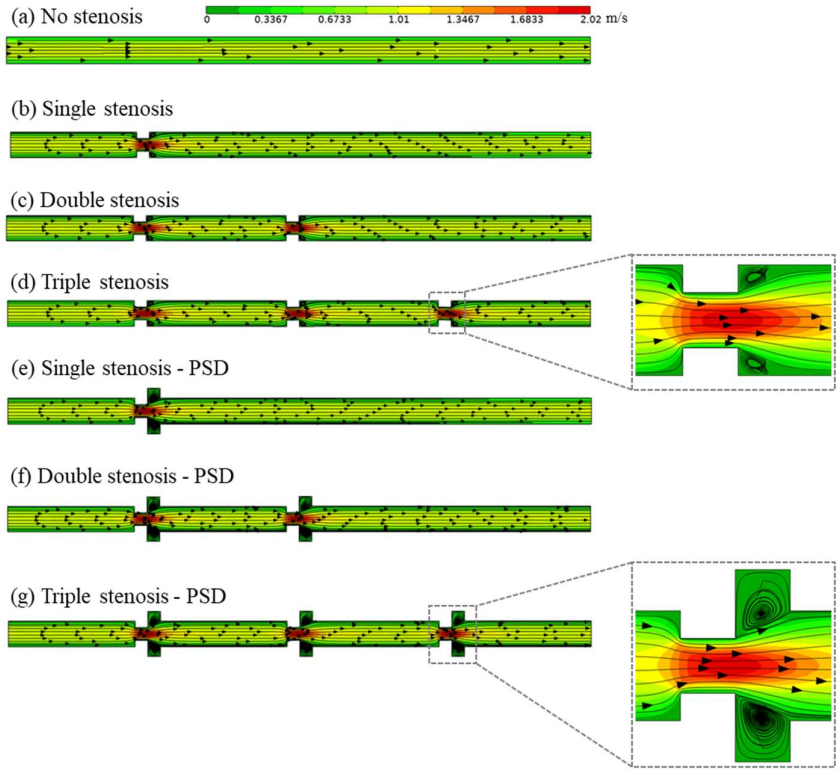

Figure 6.3: Surface velocity profile at an inlet bulk shear rate of 30,000 s^{-1} presented for different geometries: (a) healthy vessel, (b) single stenosed, (c) double stenosed, (d) triple stenosed, (e) single stenosis-PSD, (f) double stenosis-PSD, (g) triple stenosis-PSD.

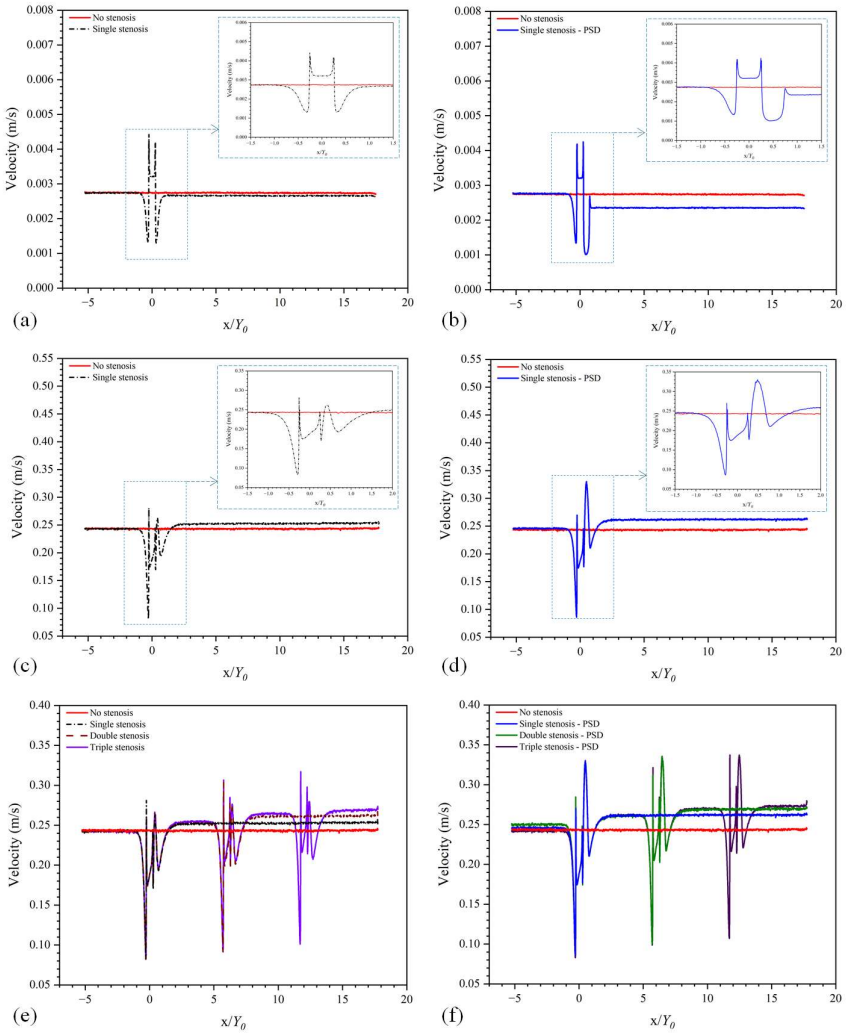

Figure 6.4: Velocity variation along the streamline passing close to the vessel wall for different stenosis configuration: (a, b) single stenosis and single stenosis with PSD at an inlet bulk shear rate of 500 s^{-1}, (c, d) single stenosis and single stenosis with PSD microvessels at an inlet bulk shear rate of 30,000 s^{-1}, (e, f) multiple stenosis and multiple stenosis with PSD at an inlet bulk shear rate of 30,000 s^{-1}. (x/Y_0 represents the non-dimensional axial length, where x is the distance along the channel and Y_0 = 200 µm is the channel width used for normalization.)

The distribution of velocity is illustrated in Figure 6.4, providing insight into how different stenosis geometries and flow conditions affect platelet dynamics. Referring to Figure 6.4(a-d), the quantitative data shows that in a healthy vessel, the variation of velocity near the wall

remains constant at all inlet flow conditions. Meanwhile, a drastic change in the flow can be observed near the wall for cases of stenosis. The graph shows a steep velocity gradient between the throat of the stenosed region and the adjacent recirculation zones. Within these recirculation zones, the local shear stress experienced by the trapped platelets tends to be relatively low but has a long residence time, meaning that platelets remain in these zones for extended durations. This combination of low shear and long residence time creates favourable conditions for already activated platelets to adhere to the vessel walls, thereby promoting thrombus formation. These results are in good agreement with the literature [34], where numerical and experimental studies have shown similar platelet behavior in gradual constriction expansion geometry. Additionally, in configurations involving multiple stenosis, platelets are subjected to repeated loading conditions as they traverse through successive constriction and expansion zones, as shown in Figure 6.4(e, f). This cyclic exposure enhances the likelihood of platelet activation and deposition along the vessel walls. Graphs from Figure 6.4(a, b) show an interesting trend, considering PSD geometries under low inlet flow conditions. These geometries trap platelets in high-strength vortices for a very long time as compared to stenotic geometry without PSD.

6.3.2 Distribution of elongation stress on platelets in stenosed and PSD microvessels

Convective acceleration occurring at the stenosis throat has been identified as a key factor imposing significant elongational stresses on passing platelets, which can contribute to their activation levels [34]. According to experimental findings of Purvis et al. (1991) [106], when platelets' membranes are subjected to elongational stretches, their activation levels increase due to higher ion permeability and improved ligand binding tendency. Therefore, our study quantitatively assessed elongational strain experienced by platelets, particularly near the vessel

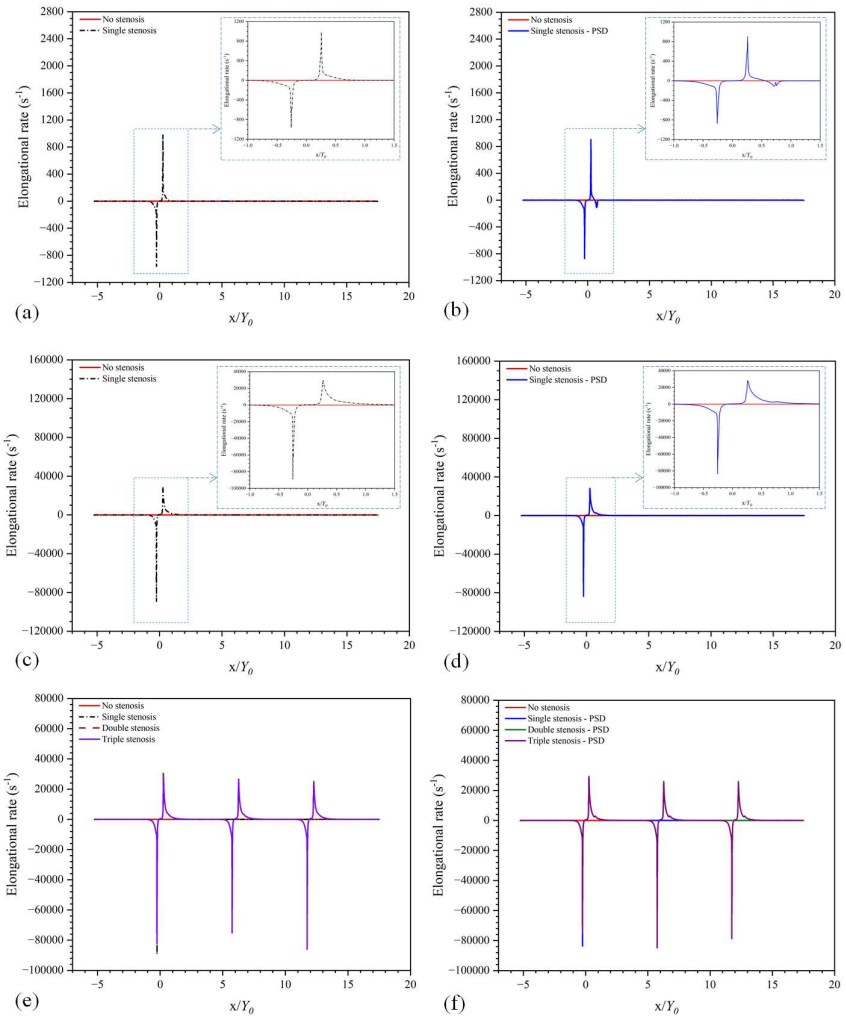

Figure 6.5: Elongation rate distribution on platelets along different stenosed geometries: (a, b) single stenosis and single stenosis with PSD microvessels at an inlet bulk shear rate of 500 s^{-1}. (c, d) single stenosis and single stenosis with PSD microvessels at an inlet bulk shear rate of 30,000 s^{-1}. (e, f) multiple stenosis and multiple stenosis with PSD at an inlet bulk shear rate of 30,000 s^{-1}.

walls, where such effects are most pronounced, as discussed in Section 6.3.1. To capture this effect, we have computed elongational strain across multiple inlet bulk shear rates (as given in Table 3). From Figure 6.5, it can be observed that for bulk shear rate of 30,000 s^{-1}, the elongational rate reaches a peak just before the flow enters the stenosis throat, reaching a negative value of -89,138.78 s^{-1}, and a positive

elongation of 29,672.16 s^{-1} as the flow reaches the beginning of expansion zone.

These findings suggest that platelets are subjected to strong compression as they accelerate through the narrow region and are stretched again in the expanding section of the vessel. In case of vessels exhibiting multiple stenoses, as platelets travel through each narrowing, mechanical stress exposure is repeated multiple times. This repeated sequence of compression and elongation cycles increases the likelihood of platelet activation and wall deposition, leading to thrombotic risk.

Interestingly, in geometries that include PSD regions, while there may not be a significant increase in elongational stress levels, the prolonged residence time within the dilatation region creates a favourable environment for platelet aggregation along the vessel wall, as shown in Figure 6.5.

6.3.3 Wall shear stress analysis on platelets in stenosed and PSD microvessels

The influence of wall shear stress across various geometries is illustrated in Figure 6.6. As observed from the figures, shear stress shows a rapid increase as flow approaches the throat of the stenosis, reaching its maximum value at the narrowest section. This peak in shear stress becomes stronger with increasing inlet flow rates. Previous studies [34] have reported that the increase in local shear stress elevates the activation potential of platelets, particularly at the site of stenosis where abrupt change in shear occurs.

Elevated shear condition induces platelet activation leading to changes in the morphology of platelets, including alterations in the shape and texture of the membrane [106]. These promote their interaction with surrounding cells and surfaces, thus promoting aggregation. In addition to elevated stress, the recirculation zones that form in the immediate downstream of the stenosis act as a favourable region for platelet aggregation as they provide prolonged residence time, allowing activated platelets to stay near to vessel wall.

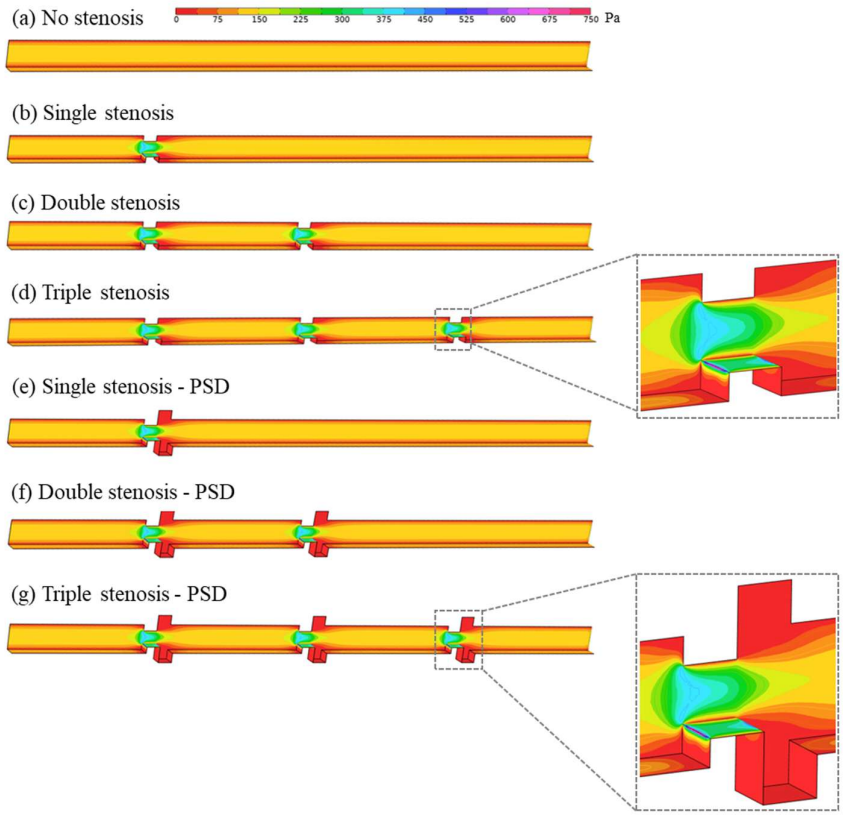

Figure 6.6: Surface distribution of shear stress for different geometries at inlet bulk shear rate of 30,000 s^{-1}: (a) healthy vessel, (b) single stenosed, (c) double stenosed, (d) triple stenosed, (e) single stenosis-PSD, (f) double stenosis-PSD, (g) triple stenosis-PSD.

Moreover, as the blood moves through the constriction region of the vessel, the frequency of hydrodynamic collisions increases between the platelet-platelet and other blood cells. These collisions, driven by the high-velocity gradients, displace the platelets from the central core of the flow towards the streamlines nearer to vessel walls and further push them into the recirculation zones [34, 105]. A similar phenomenon is observed in vessels with PSD. In these cases, vortex formation in the dilated region leads to extended trapping of platelets, further promoting their aggregation and deposition along the vessel walls. These combined mechanical and hydrodynamic effects provide a deeper understanding of how complex geometries and varying flow conditions contribute

towards the development of the thrombus in stenosed microvessels. Quantitative analysis of distribution of shear stress is shown in Figure 6.7.

As outlined in section 6.3.1, we also calculated the effect of wall shear stress at a vertical distance of 2 μm above the vessel wall to better capture the stresses experienced by the platelets travelling close to the boundary layer. Simulations were conducted for a wide range of flow rates, each corresponding to different inlet bulk shear rates (as given in Table 3). From the Figure 6.7 (a), it can be seen that at inlet bulk shear rate of 500 s^{-1} as blood flows into the stenosed segment (x/Y_0~-0.25), a sharp rise in shear stress is observed at the entrance of the narrowing, and platelets moving close to the vessel wall experiences a high shear stress over a distance of about 100 μm. Beyond the stenosed throat, at the point of flow separation, the shear stress drops rapidly, reaching values below those found in healthy vessels and remains low throughout the separation until flow further reattaches (x/Y_0~1.05).

Platelets that are activated by the intense shear stress in the stenotic region subsequently enter the expansion zone, where flow deceleration and low shear conditions allow them to become trapped within recirculation vortices. In these zones, blood velocity is greatly reduced, enabling platelets to maintain extended contact with the vessel wall. The overall effect of these shear stresses on platelets enhances their deposition at the walls.

As the inlet flow rate increases, corresponding to a bulk shear rate of 30,000 s^{-1}, a noticeable rise is observed in both the magnitude of wall shear stresses and the intensity of the recirculation zones, as illustrated in Figure 6.7(c, d). It has also been noticed that the point at which the separated flow reattaches to the vessel wall shifts further downstream, reaching $x/Y_0 \sim 2.68$ at 30,000 s^{-1}. This shift in reattachment zone with increased flow rate, indicates extension of low shear recirculation zone, thus creating a region particularly favourable for platelet trapping and aggregation.

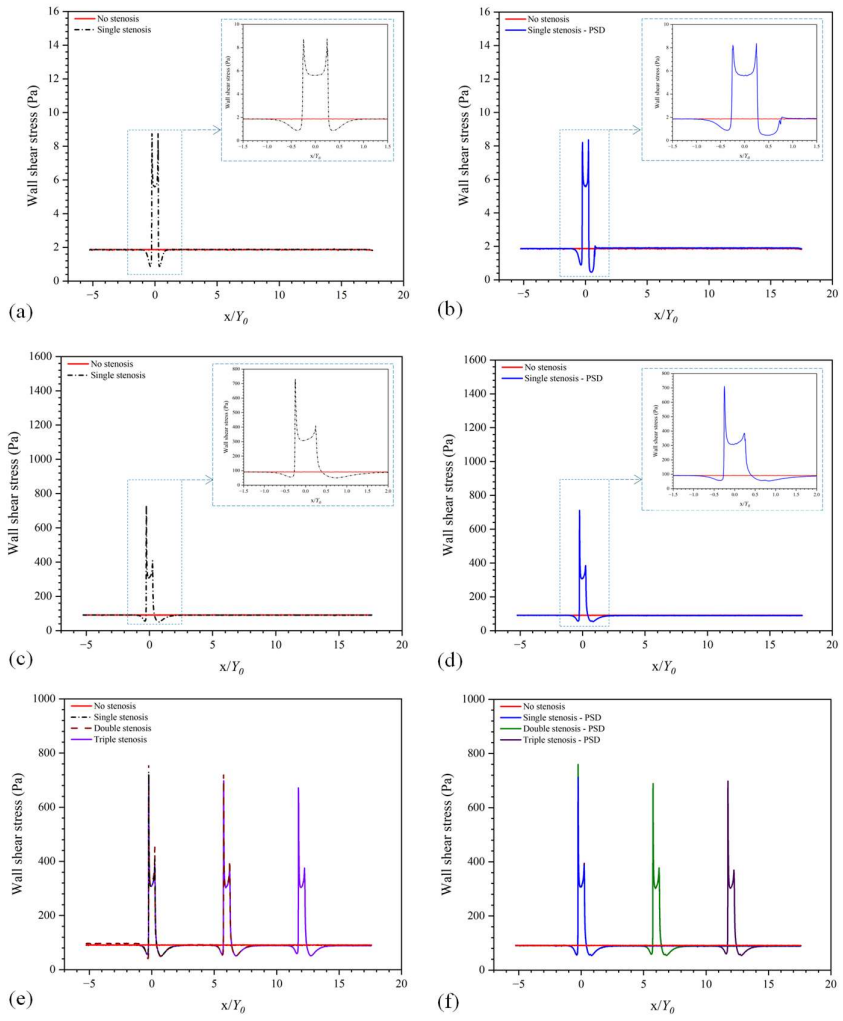

Figure 6.7: Wall shear stress distribution on platelets for various stenosed geometries: (a, b) single stenosis and single stenosis with PSD at an inlet bulk shear rate of 500 s^{-1}, (c, d) single stenosis and single stenosis at an inlet bulk shear rate of 30,000 s^{-1}, (e, f) multiple stenosis and multiple stenosis with PSD at an inlet bulk shear rate of 30,000 s^{-1}.

In the case of vessels with multiple stenoses, platelets experience repeated cycles of mechanical stress as they travel through successive constrictions. This cyclic exposure leads to increasing activation, which promotes aggregation and adhesion. A similar pattern is observed in microvessels featuring multiple stenoses combined with PSD, where the strength of recirculating vortices is even more significant than that of stenosed vessels. To quantitatively assess these effects, we have calculated the strength (ability to trap platelets) of the vortices at all inlet

bulk shear rates (as given in Table 3) for both stenosed vessel and stenosed vessel with PSD. As shown in Figure 6.8, vortex strength is consistently higher in the PSD vessels than in those without dilatation, highlighting their enhanced thrombogenic potential.

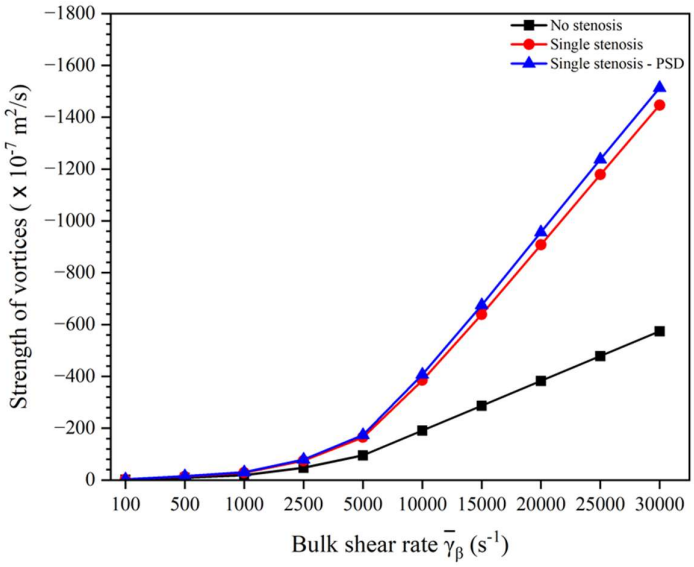

Figure 6.8: Plot representing the strength of vortices forming in the expansion zone for stenosis and stenosis with PSD microvessels.

6.4 Conclusion

In this study we have explored the influence of various hemodynamic factors affecting activation of platelets and their involvement in potential deposition at the vessel wall. We have analyzed the flow dynamics across three types of vascular configuration: healthy vessels, vessels with stenosis, and vessels with stenosis followed by post-stenotic dilatation region.

The presence of a stenosed region significantly disrupts the normal flow behavior leading to alteration in velocity fields and shear distributions. As the blood flows, it experiences transition from high shear near the stenotic throat to low shear in the downstream recirculation zones. This changes surface morphology of platelets and elevates activation potential, thereby increasing the possibility of their adhesion to vessel wall. Additionally, both stenosed and PSD microvessels exhibit steep

velocity gradients in the downstream sections, exposing near-wall platelets to elevated shear, which further contributes to platelet activation. The formation of recirculation zones at the immediate downstream of stenosis creates localized environments that favours platelet-platelet interactions. These interactions promote aggregation and enhance the likelihood of platelet deposition along the vessel wall. Quantitative analysis showed that the velocity at the stenotic throat increased by 1.6-fold relative to inlet, followed by a drop of 3.2-fold in the downstream of the throat, leading to formation of recirculation zones. Additionally, elongational stress analysis indicated compression of platelet at the throat entrance by decrement in elongational rate by ~560-folds, whereas they experience stretching as they leave the throat by a sudden increase in elongational rate by ~570-folds, when subjected to an inlet bulk shear rate of 500 s^{-1}. Further, the wall shear stress analysis suggested an 8-fold increase in shear force along the vessel wall within the stenotic segment. However, in the downstream, the wall shear stress decreases by ~14-fold in the recirculation zone, eventually approaching baseline near the reattachment region. Numerical results also indicate that microvessels with PSD have stronger recirculation zones compared to stenosed vessels, leading to longer platelet entrapment and increasing the risk of thrombus formation. These variations in wall shear stress, elongation rate, and velocity collectively enhance the platelet activation and aggregation. High shear stress at the stenosis entrance can trigger initial platelet activation, while the low shear and flow reversal within the recirculation zones at the downstream create ideal conditions for platelet adhesion and thrombus development. These hemodynamic disturbances around stenosed and PSD regions offer valuable insights into the flow mechanisms that facilitate mural thrombus formation.

Chapter 7

Conclusion and Future Scope

7.1 Highlights of new concepts and innovations

In this thesis, we have conducted a comprehensive investigation to understand the effect of microvascular geometries and flow conditions on blood flow behavior that leads to mural thrombus formation. One of the key highlights of this study is our use of low-cost SLA 3D printing to create microfluidic device molds, followed by PDMS soft lithography to fabricate the microfluidic device. This approach enabled us to fabricate the device in cost effective manner, which was later used to validate our computational methodology.

Another important aspect of our work is systematically exploration of geometrical variations of stenosed geometry on local hemodynamics using CFD simulations. Stenosis severity, angular variation, curvature radius alters shear distribution, recirculation strength, and platelet residence time, all of which are key contributors towards thrombus initiation and growth. We also compared healthy, stenosed, and post-stenotic dilatation (PSD) blood vessels. The PSD configurations showed more intense and prolonged recirculation, posing a higher risk for platelet accumulation and thrombus formation.

7.2 Summary of key findings

From our detailed numerical investigation, we arrived at several key findings:

- Effect of shear and recirculation - We observed that higher bulk shear rates significantly elevate the local shear distribution and enhance the strength of recirculation zones, both of which favour platelet activation.
- Impact of stenosis severity - As the degree of stenosis increased from 50% to 87.5%, the local shear rate sharply elevates by ~12-folds in

the stenosed region. This led to stronger downstream recirculation, thereby increasing platelet residence time and adhesion potential.

- Influence of geometry - Our simulation showed that angular topology significantly affects inlet and exit flow behavior, with smoother exit angles minimizing vortex formation, thus decreasing the likelihood of platelet trapping, while larger curvature radius at the stenosis throat was found to reduce shear distribution and shift the recirculation zone closer to the vessel wall, potentially lowering thrombosis risk.
- Post-stenotic dilatation (PSD) effects - The PSD geometries exhibited prolonged low-shear recirculation regions, making them highly thrombogenic compared to healthy or stenosed vessels. When multiple stenoses were considered, we found that velocity peaks occur at each constriction, resulting in alternating high- and low-velocity zones that amplify flow instability and recirculation.
- Elongational strain and platelet mechanics - We also found that platelets undergo abrupt changes in deformation forces, including compression before the stenosis, and stretching post-stenosis. These mechanical fluctuations can lead to platelet deformation and initiate activation pathways. The coexistence of high shear near the throat and low shear downstream provides favourable conditions for platelet adhesion and aggregation thus leading to formation of mural thrombosis.

Through these analyses, we have gained a better picture showing the effect of geometric variations on flow structures and stress environments within the vessels. This study has deepened our understanding of the mechanical aspects of platelet activation and offers insight into the formation of mural thrombus in stenosed vessels.

7.3 Key improvements from the literature

Previous studies have primarily used microfluidic devices with stenoses to investigate platelet activation, aggregation, and thrombus formation under disturbed flow conditions. These investigations have established

that hemodynamic factors such as wall shear stress, shear rate and its gradients, recirculation zones, and velocity variations play a critical role in thrombus formation. Most of these works have used idealized stenosis shapes, such as circular or trapezoidal constrictions. However, the influence of geometrical variations of stenosed region on local hemodynamics, which is key to governing platelet behavior has not been extensively explored despite its fundamental importance in vascular pathology and blood-wetted medical devices.

In our work, we have extended this understanding by systematically studying the interaction between microvascular geometry, flow conditions, and their possible effect on platelet behavior. We found that increased bulk shear rates and narrower stenoses amplify local shear and downstream recirculation, directly affecting platelet activation and aggregation. Angular topology and radial curvature were found to influence flow stability and vortex formation, modulating platelet residence time and thrombotic potential. In cases involving multiple stenoses and PSD regions, repeated compression-elongation cycles and prolonged platelet trapping in downstream vortices significantly enhance thrombus growth and deposition. PSD geometries are comparatively more prone to thrombosis than single stenoses, as the downstream vortices trap platelets in low-shear zones, promoting aggregation and deposition despite lower shear than at the stenosis throat.

Through this study, we have provided a more comprehensive understanding of flow-driven thrombus formation by bridging the relationship between microvascular geometry, hemodynamics, and platelet mechanics. Our findings offer insights into the flow physics underlying thrombus formation through microfluidic platforms.

7.4 Vision for future work

This study offers valuable insight into the mural thrombosis mechanism, it also lays the groundwork for exploring new directions in future studies. In the present study, we have modelled blood as a continuum

fluid to simplify the simulation process and maintain computational feasibility across a wide range of microvascular geometries. While this approach is commonly used and effective for capturing general hemodynamic trends, we believe that considering cell-resolved simulations or multiphase modelling in future studies can provide a better representation of flow dynamics, particularly in regions of disturbed flow, such as recirculation zones.

Additionally, incorporating advanced rheological models such as population balance or viscoelastic (like Generalized Oldroyd-B), or mixture theory-based approach could enhance our understanding of the complex rheological behavior of blood constituents in thrombus formation within stenosed geometries. This can help build better simulation to predict the risk of clot formation in blood vessels and improve the design of medical devices like stents, grafts, etc. to minimize stagnation zones and recirculation that often promotes thrombosis.

References

1. Whitesides G. M., (2006), The Origins and the Future of Microfluidics, Nature, 442 (7101), 368-373 (DOI: 10.1038/nature05058)
2. Sackmann E. K., Fulton A. L., Beebe D. J., (2014), The Present and Future Role of Microfluidics in Biomedical Research, Nature, 507 (7491), 181-189 (DOI: 10.1038/nature13118)
3. Beverung S., Wu J., Steward R., (2020), Lab-on-a-Chip for Cardiovascular Physiology and Pathology, Micromachines, 11 (10), 898 (DOI: 10.3390/mi11100898)
4. Ren J., Wang Z., Du N., Cheng W., Ju L. A., (2024), Charting the Course of Blood Flow: Vessel-on-a-Chip Technologies in Thrombosis Studies, Microstructures, 4 (3) (DOI: 10.20517/microstructures.2023.106)
5. Rajendran P., Rengarajan T., Thangavel J., Nishigaki Y., Sakthisekaran D., Sethi G., Nishigaki I, (2013), The Vascular Endothelium and Human Diseases, Int. J. Biol. Sci., 9 (10), 1057-1069 (DOI: 10.7150/ijbs.7502)
6. Neubauer K., Zieger B., (2022), Endothelial Cells and Coagulation, Cell Tissue Res., 387 (3), 391-398 (DOI: 10.1007/s00441-021-03471-2)
7. Ha H., Lee S.-J., (2013), Hemodynamic Features and Platelet Aggregation in a Stenosed Microchannel, Microvasc. Res., 90, 96-105 (DOI: 10.1016/j.mvr.2013.08.008)
8. Rana A., Westein E., Niego B., Hagemeyer C. E., (2019), Shear-Dependent Platelet Aggregation: Mechanisms and Therapeutic Opportunities, Front. Cardiovasc. Med., 6 (DOI: 10.3389/fcvm.2019.00141)
9. Wang S., Griffith B. P., Wu Z. J., (2021), Device-Induced Hemostatic Disorders in Mechanically Assisted Circulation, Clin. Appl. Thromb./Hemost., 27 (DOI: 10.1177/1076029620982374)

10. Flores Marcial H. B., Choi J., Ham D., Kim J., Jeong P., Choi J., Park W.-T., (2022), Influence of Multiple Stenoses on Thrombosis Formation: An in Vitro Study, Micro Nano Syst. Lett., 10 (1), 18 (DOI: 10.1186/s40486-022-00159-2)
11. Shabbir M. S., Ali N., Abbas Z., (2018), Unsteady Blood Flow of Non-Newtonian Fluid through a Rigid Artery in the Presence of Multi-Irregular Stenoses, J. Braz. Soc. Mech. Sci. Eng., 40 (9), 413 (DOI: 10.1007/s40430-018-1327-x)
12. Kabir Md. A., Alam Md. F., Uddin Md. A., (2021), Numerical Simulation of Pulsatile Blood Flow: A Study with Normal Artery, and Arteries with Single and Multiple Stenosis, J. Eng. Appl. Sci., 68 (1), 24 (DOI: 10.1186/s44147-021-00025-9)
13. Hoffman M., Monroe D., (2001), A Cell-Based Model of Hemostasis, Thromb Haemost, 85 (06), 958-965 (DOI: 10.1055/s-0037-1615947)
14. Mackman N., (2008), Triggers, Targets and Treatments for Thrombosis, Nature, 451 (7181), 914-918 (DOI: 10.1038/nature06797)
15. Hadi H. A. R., Carr C. S., Al Suwaidi J., (2005), Endothelial Dysfunction: Cardiovascular Risk Factors, Therapy, and Outcome, Vasc. Health Risk Manag., 1 (3), 183-198 (DOI: 10.2147/vhrm.s12187331)
16. Kumar D. R., Hanlin E., Glurich I., Mazza J. J., Yale S. H., (2010), Virchow's Contribution to the Understanding of Thrombosis and Cellular Biology, Clin. Med. Res., 8 (3-4), 168-172. (DOI: 10.3121/cmr.2009.866)
17. Created with BioRender.com.
18. Tucker W. D., Arora Y., Mahajan K., (2025), Anatomy, Blood Vessels (PMID: 29262226)
19. Camasão D. B., Mantovani D., (2021), The Mechanical Characterization of Blood Vessels and Their Substitutes in the Continuous Quest for Physiological-Relevant Performances A Critical Review, Mater. Today. Bio., 10, 100106 (DOI: 10.1016/j.mtbio.2021.100106)

20. Pober J. S., Sessa W. C., (2007), Evolving Functions of Endothelial Cells in Inflammation. Nat. Rev. Immunol., 7 (10), 803-815 (DOI: 10.1038/nri2171)
21. Libby P., Ridker P. M., Hansson G. K., (2011), Progress and Challenges in Translating the Biology of Atherosclerosis, Nature, 473 (7347), 317-325. (DOI: 10.1038/nature10146)
22. Davies P. F., (2009), Hemodynamic Shear Stress and the Endothelium in Cardiovascular Pathophysiology, Nat. Clin. Pract. Cardiovasc. Med., 6 (1), 16-26 (DOI: 10.1038/ncpcardio1397)
23. Casa L. D. C., Ku D. N., (2017), Thrombus Formation at High Shear Rates, Annu. Rev. Biomed. Eng.,19 (1), 415-433 (DOI: 10.1146/annurev-bioeng-071516-044539)
24. Yang Y., Song Y., Mu X., (2024), The Role of Fluid Mechanics in Coronary Atherosclerotic Plaques: An Up-to-Date Review, Rev. Cardiovasc. Med., 25 (2) (DOI: 10.31083/j.rcm2502049)
25. Tangelder G. J., Teirlinck H. C., Slaaf D. W., Reneman R. S., (1985), Distribution of Blood Platelets Flowing in Arterioles, Am. J. Physiol. - Heart Circ. Physiol., 248 (3), H318–H323 (DOI: 10.1152/ajpheart.1985.248.3.H318)
26. Woldhuis B., Tangelder G. J., Slaaf D. W., Reneman, R. S., (1992), Concentration Profile of Blood Platelets Differs in Arterioles and Venules, Am. J. Physiol. - Heart Circ. Physiol., 262 (4), H1217–H1223 (DOI: 10.1152/ajpheart.1992.262.4.H1217)
27. Zhou Z., Nguyen T., Guchhait P., Dong, J. Von Willebrand Factor, (2010), ADAMTS-13, and Thrombotic Thrombocytopenic Purpura, Semin Thromb Hemost, 36 (01), 071–081 (DOI: 10.1055/s-0030-1248726)
28. Casa L. D. C., Deaton D. H., Ku D. N., (2015), Role of High Shear Rate in Thrombosis, J. Vasc. Surg., 61 (4), 1068–1080 (DOI: 10.1016/j.jvs.2014.12.050)

29. Jackson S. P., (2007), The Growing Complexity of Platelet Aggregation, Blood, 109 (12), 5087-5095 (DOI: 10.1182/blood-2006-12-027698)
30. Ruggeri, Z. M., (2002), Platelets in Atherothrombosis, Nat. Med., 8 (11), 1227–1234. (DOI: 10.1038/nm1102-1227)
31. Asada Y., Yamashita A., Sato Y., Hatakeyama K., (2020), Pathophysiology of Atherothrombosis: Mechanisms of Thrombus Formation on Disrupted Atherosclerotic Plaques, Pathol. Int., 70 (6), 309–322 (DOI: 10.1111/pin.12921)
32. Fogelson A. L., Neeves K. B., (2015), Fluid Mechanics of Blood Clot Formation, Annu. Rev. Fluid. Mech., 47 (1), 377–403 (DOI: 10.1146/annurev-fluid-010814-014513)
33. Young D. F., Tsai F. Y., (1973), Flow Characteristics in Models of Arterial Stenoses — I. Steady Flow, J. Biomech., 6 (4), 395–410 (DOI: 10.1016/0021-9290(73)90099-7)
34. Bluestein D., Niu L., Schoephoerster R. T., Dewanjee M. K., (1997), Fluid Mechanics of Arterial Stenosis: Relationship to the Development of Mural Thrombus, Ann. Biomed. Eng., 25 (2), 344–356 (DOI: 10.1007/BF02648048)
35. Schneider S. W., Nuschele S., Wixforth A., Gorzelanny C., Alexander-Katz A., Netz R. R., Schneider, M. F., (2007), Shear-Induced Unfolding Triggers Adhesion of von Willebrand Factor Fibers, Proc. Natl. Acad. Sci. U. S. A., 104 (19), 7899–7903 (DOI: 10.1073/pnas.0608422104)
36. Nesbitt W. S., Westein E., Tovar-Lopez F. J., Tolouei E., Mitchell A., Fu J., Carberry J., Fouras A., Jackson S. P. A, (2009), Shear Gradient–Dependent Platelet Aggregation Mechanism Drives Thrombus Formation, Nat. Med., 15 (6), 665–673 (DOI: 10.1038/nm.1955)
37. Tovar-Lopez F. J., Rosengarten G., Khoshmanesh K., Westein E., Jackson S. P., Nesbitt W. S., Mitchell A., (2011), Structural and Hydrodynamic Simulation of an Acute Stenosis-Dependent Thrombosis Model in Mice, J. Biomech., 44 (6), 1031–1039 (DOI: 10.1016/j.jbiomech.2011.02.006)

38. Westein E., Van der Meer A. D., Kuijpers M. J. E., Frimat J.-P., Van den Berg A., Heemskerk J. W. M., (2013), Atherosclerotic Geometries Exacerbate Pathological Thrombus Formation Poststenosis in a von Willebrand Factor-Dependent Manner, Proc. Natl. Acad. Sci. U. S. A., 110 (4), 1357–1362 (DOI: 10.1073/pnas.1209905110)
39. Brazilek R. J., Tovar-Lopez F. J., Wong A. K. T., Tran H., Davis A. S., McFadyen J. D., Kaplan Z., Chunilal S., Jackson S. P., Nandurkar H., Mitchell A., Nesbitt W. S., (2017), Application of a Strain Rate Gradient Microfluidic Device to von Willebrand's Disease Screening, Lab Chip, 17 (15), 2595–2608 (DOI: 10.1039/C7LC00498B)
40. Ting L. H., Feghhi S., Taparia N., Smith A. O., Karchin A., Lim E., John A. St., Wang X., Rue T., White N. J., Sniadecki N. J., (2019), Contractile Forces in Platelet Aggregates under Microfluidic Shear Gradients Reflect Platelet Inhibition and Bleeding Risk, Nat. Commun., 10 (1), 1204 (DOI: 10.1038/s41467-019-09150-9)
41. Receveur N., Nechipurenko D., Knapp Y., Yakusheva A., Maurer E., Denis CV., Lanza F., Panteleev M., Gachet C., Mangin PH., (2020), Shear rate gradients promote a bi-phasic thrombus formation on weak adhesive proteins, such as fibrinogen in a VWF-dependent manner, Haematologica, 105(10):2471-2483 (DOI: 10.3324/haematol.2019.235754)
42. Menon N. V., Su C., Pang K. T., Phua Z. J., Tay H. M., Dalan R., Wang X., Li K. H. H., Hou H. W., (2020), Recapitulating Atherogenic Flow Disturbances and Vascular Inflammation in a Perfusable 3D Stenosis Model, Biofabrication, 12 (4), 045009 (DOI: 10.1088/1758-5090/aba501)
43. Zhao Y. C., Vatankhah P., Goh T., Michelis R., Kyanian K., Zhang Y., Li Z., Ju L. A., (2021), Hemodynamic Analysis for Stenosis Microfluidic Model of Thrombosis with Refined Computational Fluid Dynamics Simulation, Sci. Rep., 11 (1), 6875 (DOI: 10.1038/s41598-021-86310-2)

44. Ham D.-H., Choi J.-S., Jeong P.-H., Kim J.-H., Flores Marcial H. B., Choi J.-H., Park W.-T., (2023), Analysis of Thrombosis Formation and Growth Using Microfluidic Chips and Multiphase Computational Fluid Dynamics, Biochip J., 17 (4), 478–486 (DOI: 10.1007/s13206-023-00123-1)
45. Jain A., Graveline A., Waterhouse A., Vernet A., Flaumenhaft R., Ingber D. E., (2016), A Shear Gradient-Activated Microfluidic Device for Automated Monitoring of Whole Blood Haemostasis and Platelet Function, Nat. Commun., 7 (1), 10176 (DOI: 10.1038/ncomms10176)
46. Zainal Abidin N. A., Poon E. K. W., Szydzik C., Timofeeva M., Akbaridoust F., Brazilek R. J., Tovar Lopez F. J., Ma X., Lav C., Marusic I., Thompson P. E., Mitchell A., Ooi A. S. H., Hamilton J. R., Nesbitt W. S., (2022) An Extensional Strain Sensing Mechanosome Drives Adhesion-Independent Platelet Activation at Supraphysiological Hemodynamic Gradients, BMC Biol., 20 (1), 73 (DOI: 10.1186/s12915-022-01274-7)
47. Costa P. F., Albers H. J., Linssen J. E. A., Middelkamp H. H. T., van der Hout L., Passier R., van den Berg A., Malda J., van der Meer A. D., (2017), Mimicking Arterial Thrombosis in a 3D-Printed Microfluidic in Vitro Vascular Model Based on Computed Tomography Angiography Data, Lab Chip, 17 (16), 2785–2792 (DOI: 10.1039/C7LC00202E)
48. Berry J., Peaudecerf F. J., Masters N. A., Neeves K. B., Goldstein R. E., Harper M. T., (2021), An “Occlusive Thrombosis-on-a-Chip” Microfluidic Device for Investigating the Effect of Anti-Thrombotic Drugs, Lab Chip, 21 (21), 4104–4117. (DOI: 10.1039/D1LC00347J)
49. Ciciliano J. C., Sakurai Y., Myers D. R., Fay M. E., Hechler B., Meeks S., Li R., Dixon J. B., Lyon L. A., Gachet C., Lam W. A., (2015), Resolving the Multifaceted Mechanisms of the Ferric Chloride Thrombosis Model Using an Interdisciplinary Microfluidic Approach, Blood, 126 (6), 817–824 (DOI: 10.1182/blood-2015-02-628594)

50. Zhang Y., Aye S., Cheng V., Nasser A., Hong T., Vatankhah P., Jiang F., Zhao Y. C., Moldovan L., Sun A., Dupuy A., Wang Y., Li Z., Ang T., Passam F., Yong K., Ju L. A., (2023), Microvasculature-on-a-Post Chip That Recapitulates Prothrombotic Vascular Geometries and 3D Flow Disturbance, Adv. Mater. Interfaces., 10 (29) (DOI: 10.1002/admi.202300234)
51. Nejad A. A., Talebi Z., Cheraghali D., Shahbani-Zahiri A., Norouzi M., (2018), Pulsatile Flow of Non-Newtonian Blood Fluid inside Stenosed Arteries: Investigating the Effects of Viscoelastic and Elastic Walls, Arteriosclerosis, and Polycythemia Diseases, Comput. Methods Programs Biomed., 154, 109–122 (DOI: 10.1016/j.cmpb.2017.11.016)
52. Baskurt O.K., Meiselman H.J., (2003), Blood Rheology and Hemodynamics, Semin Thromb Hemost, 29 (5) 435-450 (DOI: 10.1055/s-2003-44551)
53. Ascolese M., Farina A., Fasano A., (2019), The Fåhræus-Lindqvist Effect in Small Blood Vessels: How Does It Help the Heart? J. Biol. Phys., 45 (4), 379–394 (DOI: 10.1007/s10867-019-09534-4)
54. Shibeshi S. S., Collins W. E., (2005), The Rheology of Blood Flow in a Branched Arterial System, Appl. Rheol., 15 (6), 398-405 (DOI: 10.1515/arh-2005-0020)
55. Johnston B. M., Johnston P. R., Corney S., Kilpatrick D., (2006), Non-Newtonian Blood Flow in Human Right Coronary Arteries: Transient Simulations, J. Biomech., 39 (6), 1116–1128 (DOI: 10.1016/j.jbiomech.2005.01.034)
56. Siauw W. L., Ng E. Y. K., Mazumdar J., (2000), Unsteady Stenosis Flow Prediction: A Comparative Study of Non-Newtonian Models with Operator Splitting Scheme, Med. Eng. Phys., 22 (4), 265–277 (DOI: 10.1016/S1350-4533(00)00036-9)
57. Morbiducci U., Gallo D., Massai D., Ponzini R., Deriu M. A., Antiga L., Redaelli A., Montevecchi F. M., (2011), On the Importance of Blood Rheology for Bulk Flow in Hemodynamic

Models of the Carotid Bifurcation, J. Biomech., 44 (13), 2427–2438 (DOI: 10.1016/j.jbiomech.2011.06.028)

58. Razavi A., Shirani E., Sadeghi M. R., (2011), Numerical Simulation of Blood Pulsatile Flow in a Stenosed Carotid Artery Using Different Rheological Models, J. Biomech., 44 (11), 2021–2030 (DOI: 10.1016/j.jbiomech.2011.04.023)
59. Boyd J., Buick J. M., Green S., (2007), Analysis of the Casson and Carreau-Yasuda Non-Newtonian Blood Models in Steady and Oscillatory Flows Using the Lattice Boltzmann Method, Phys. Fluids, 19 (9) (DOI: 10.1063/1.2772250)
60. Jariwala S., Horner J. S., Wagner N. J., Beris A. N., (2020), Application of Population Balance-Based Thixotropic Model to Human Blood, J. Non-Newton. Fluid Mech., 281, 104294 (DOI: 10.1016/j.jnnfm.2020.104294)
61. Krystian J., Łukasz M., Wojciech O., (2023), Model of Blood Rheology Including Hemolysis Based on Population Balance, Commun. Nonlinear Sci. Numer. Simul., 116, 106802 (DOI: 10.1016/j.cnsns.2022.106802)
62. Anand M., Kwack J., Masud A., (2013), A New Generalized Oldroyd-B Model for Blood Flow in Complex Geometries, Int. J. Eng. Sci., 72, 78-88 (DOI: 10.1016/j.ijengsci.2013.06.009)
63. Yeleswarapu K. K., Kameneva M. V., Rajagopal K. R., Antaki J. F., (1998), The Flow of Blood in Tubes: Theory and Experiment, Mech. Res. Commun., 25 (3), 257-262 (DOI: 10.1016/S0093-6413(98)00036-6)
64. Wu W.-T., Aubry N., Massoudi M., Kim J., Antaki J. F., (2014), A Numerical Study of Blood Flow Using Mixture Theory, Int. J. Eng. Sci., 76, 56-72 (DOI: 10.1016/j.ijengsci.2013.12.001)
65. Ahmad R., Farooqi A., Farooqi R., Hamadneh N. N., Fayz-Al-Asad M., Khan I., Sajid M., Bary G., Saleem Khan M. F., (2021), An Analytical Approach to Study the Blood Flow over a Nonlinear Tapering Stenosed Artery in Flow of Carreau Fluid Model, Complexity, 2021 (1) (DOI: 10.1155/2021/9921642)

66. Umadevi C., Dhange M., Haritha B., Sudha T., (2021), Flow of Blood Mixed with Copper Nanoparticles in an Inclined Overlapping Stenosed Artery with Magnetic Field, Case Stud. Therm. Eng., 25, 100947 (DOI: 10.1016/j.csite.2021.100947)
67. Alsemiry R. D., Sayed H. M., Amin N., (2022), Mathematical Analysis of Carreau Fluid Flow and Heat Transfer within an Eccentric Catheterized Artery, AEJ - Alex. Eng. J., 61 (1), 523-539 (DOI: 10.1016/j.aej.2021.06.029)
68. Zaman A., Khan A. A., (2021), Time Dependent Non-Newtonian Nano-Fluid (Blood) Flow in w-Shape Stenosed Channel, with Curvature Effects, Math. Comput. Simul., 181, 82-97 (DOI: 10.1016/j.matcom.2020.09.017)
69. Wajihah S. A., Sankar D. S., (2023), A Review on Non-Newtonian Fluid Models for Multi-Layered Blood Rheology in Constricted Arteries, Arch. Appl. Mech., 93 (5), 1771-1796 (DOI: 10.1007/s00419-023-02368-6)
70. Miller C., (1972), Predicting Non-Newtonian Flow Behavior in Ducts of Unusual Cross Section, Ind. Eng. Chem. Fundamen., 11 (4), 524-528 (DOI: 10.1021/i160044a015)
71. Zhao, Y.C., Vatankhah, P., Goh, T., Wang, J., Chen, X.V., Kashani, M.N., Zheng, K., Li, Z. and Ju, L.A., (2021), Computational fluid dynamics simulations at micro-scale stenosis for microfluidic thrombosis model characterization, MCB Molecular and Cellular Biomechanics, 18(1), pp.1-10 (DOI: 10.32604/mcb.2021.012598)
72. White F. M., (2011), Viscous Flow in Ducts. Fluid Mechanics, McGraw-Hill, 347-456
73. Hajam M. I., Khan M. M., (2024), Microfluidics: A Concise Review of the History Principles Design Applications and Future Outlook, Biomater. Sci., 12 (2), 218-251 (DOI: 10.1039/D3BM01463K)
74. Lojek B., (2007), The MOS Transistor, In History of Semiconductor Engineering, Springer Berlin Heidelberg: Berlin Heidelberg, 317-374 (DOI: 10.1007/978-3-540-34258-8_11)

75. Terry S. C., Jerman J. H., Angell J. B., (1979), A Gas Chromatographic Air Analyzer Fabricated on a Silicon Wafer, IEEE Trans Electron Devices, 26 (12), 1880-1886 (DOI: 10.1109/T-ED.1979.19791)
76. Cavalli-Sforza L. L., (2005), The Human Genome Diversity Project: Past Present and Future, Nat. Rev. Genet., 6 (4), 333-340 (DOI: 10.1038/nrg1596)
77. Xia Y., Whitesides G. M., (1998), Soft Lithography, Angew. Chem. - Int. Ed., 37 (5), 550-575 (DOI: 10.1002/(SICI)1521-3773(19980316)37:5<550::AID-ANIE550>3.0.CO,2-G)
78. Scott S., Ali Z., (2021), Fabrication Methods for Microfluidic Devices: An Overview, Micromachines, 12 (3), 319 (DOI: 10.3390/mi12030319)
79. Cao U. M. N., Zhang Y., Chen J., Sayson D., Pillai S., Tran S. D., (2023), Microfluidic Organ-on-A-Chip: A Guide to Biomaterial Choice and Fabrication, Int. J. Mol. Sci., 24 (4), 3232 (DOI: 10.3390/ijms24043232)
80. Niculescu A.-G., Chircov C., Bîrcă A. C., Grumezescu A. M., (2021), Fabrication and Applications of Microfluidic Devices: A Review, Int. J. Mol. Sci., 22 (4), 2011 (DOI: 10.3390/ijms22042011)
81. Ren K., Zhou J., Wu H., (2013), Materials for Microfluidic Chip Fabrication, Acc. Chem. Res., 46 (11), 2396-2406 (DOI: 10.1021/ar300314s)
82. Martins J. P., Torrieri G., Santos H. A., (2018), The Importance of Microfluidics for the Preparation of Nanoparticles as Advanced Drug Delivery Systems, Expert. Opin. Drug. Deliv., 15 (5), 469-479 (DOI: 10.1080/17425247.2018.1446936)
83. Nielsen J. B., Hanson R. L., Almughamsi H. M., Pang C., Fish T. R., Woolley A. T., (2020), Microfluidics: Innovations in Materials and Their Fabrication and Functionalization, Anal. Chem., 92 (1), 150-168 (DOI: 10.1021/acs.analchem.9b04986)
84. Kotz F., Mader M., Dellen N., Risch P., Kick A., Helmer D., Rapp B., (2020), Fused Deposition Modeling of Microfluidic

Chips in Polymethylmethacrylate, Micromachines, 11 (9), 873 (DOI: 10.3390/mi11090873)

85. Bruijns B., Veciana A., Tiggelaar R., Gardeniers H., (2019), Cyclic Olefin Copolymer Microfluidic Devices for Forensic Applications. Biosensors, 9 (3), 85 (DOI: 10.3390/bios9030085)
86. Nielsen J. B., Hanson R. L., Almughamsi H. M., Pang C., Fish T. R., Woolley A. T., (2020), Microfluidics: Innovations in Materials and Their Fabrication and Functionalization, Anal. Chem., 92 (1), 150-168 (DOI: 10.1021/acs.analchem.9b04986)
87. Hwang J., Cho Y. H., Park M. S., Kim B. H., (2019), Microchannel Fabrication on Glass Materials for Microfluidic Devices, Int. J. Precis. Eng. Manuf., 20 (3), 479-495 (DOI: 10.1007/s12541-019-00103-2)
88. Wlodarczyk K. L., Hand D. P., Maroto-Valer M. M., (2019), Maskless Rapid Manufacturing of Glass Microfluidic Devices Using a Picosecond Pulsed Laser, Sci. Rep., 9 (1), 20215 (DOI: 10.1038/s41598-019-56711-5)
89. Kajtez J., Buchmann S., Vasudevan S., Birtele M., Rocchetti S., Pless C. J., Heiskanen A., Barker R. A., Martínez-Serrano A., Parmar M., Lind J. U., Emnéus J., (2020), 3D-Printed Soft Lithography for Complex Compartmentalized Microfluidic Neural Devices, Adv. Sci., 7 (16) (DOI: 10.1002/advs.202001150)
90. Choi S. Y., Habimana O., Flood P., Reynaud E. G., Rodriguez B. J., Zhang N., Casey E., Gilchrist M. D., (2016), Material- and Feature-Dependent Effects on Cell Adhesion to Micro Injection Moulded Medical Polymers, Colloids Surf. B: Biointerfaces, 145, 46-54 (DOI: 10.1016/j.colsurfb.2016.04.032)
91. Jeon J. S., Chung S., Kamm R. D., Charest J. L., (2011), Hot Embossing for Fabrication of a Microfluidic 3D Cell Culture Platform. Biomed. Microdevices, 13 (2), 325-333 (DOI: 10.1007/s10544-010-9496-0)
92. Monia Kabandana G. K., Zhang T., Chen C., (2022), Emerging 3D Printing Technologies and Methodologies for Microfluidic

Development, Anal. Methods., 14 (30), 2885-2906 (DOI: 10.1039/D2AY00798C)

93. Ma Q., Ma H., Xu F., Wang X., Sun W., (2021), Microfluidics in Cardiovascular Disease Research: State of the Art and Future Outlook, Microsyst. Nanoeng., 7 (1), 19 (DOI: 10.1038/s41378-021-00245-2)
94. Howells O., Blayney G. J., Gualeni B., Birchall J. C., Eng P. F., Ashraf H., Sharma S., Guy O. J., (2022), Design Fabrication and Characterisation of a Silicon Microneedle Array for Transdermal Therapeutic Delivery Using a Single Step Wet Etch Process, Eur. J. Pharm. Biopharm., 171, 19-28 (DOI: 10.1016/j.ejpb.2021.06.005)
95. Fülöp G., d'Hollosy S., Hofstetter L., Baumgartner A., Nygård J., Schönenberger C., Csonka S., (2016), Wet Etch Methods for InAs Nanowire Patterning and Self-Aligned Electrical Contacts, Nanotechnology, 27 (19), 195303 (DOI: 10.1088/0957-4484/27/19/195303)
96. Morozov I. A., Gudovskikh A. S., Kudryashov D. A., Kotlyar K. P., Shubina K. Y., (2018), Effect of Temperature on Dry Etching of III-V Structures, J. Phys. Conf. Ser., 1124 041031 (DOI: 10.1088/1742-6596/1124/4/041031)
97. Silverio V., Cardoso de Freitas S., (2017), Microfabrication Techniques for Microfluidic Devices, In Complex Fluid-Flows in Microfluidics, Springer International Publishing: Cham, pp 25–51 (DOI: 10.1007/978-3-319-59593-1_2)
98. Cameron N. S., Ott A., Roberge H., Veres T., (2006), Chemical Force Microscopy for Hot-Embossing Lithography Release Layer Characterization, Soft Matter, 2 (7), 553 (DOI: 10.1039/b600936k)
99. Li L., Chan M.-K., Lee W.-B., Ng M.-C., Chan K.-L., (2019), Modeling and Experimental Performance Analysis of a Novel Heating System and Its Application to Glass Hot Embossing Technology, Opt. Lett., 44 (14), 3454 (DOI: 10.1364/OL.44.003454)

100. Ding Y., Hassan M. H., Bakker O., Hinduja S., Bártolo P., (2021), A Review on Microcellular Injection Moulding, Materials, 14 (15), 4209 (DOI: 10.3390/ma14154209)
101. Lee Y., Choi J. W., Yu J., Park D., Ha J., Son K., Lee S., Chung M., Kim H.-Y., Jeon N. L., (2018), Microfluidics within a Well: An Injection-Molded Plastic Array 3D Culture Platform, Lab Chip, 18 (16), 2433-2440 (DOI: 10.1039/C8LC00336J)
102. Wlodarczyk K., Carter R., Jahanbakhsh A., Lopes A., Mackenzie M., Maier R., Hand D., Maroto-Valer M., (2018), Rapid Laser Manufacturing of Microfluidic Devices from Glass Substrates, Micromachines, 9 (8), 409 (DOI: 10.3390/mi9080409)
103. Brousseau E. B., Dimov S. S., Pham D. T., (2010), Some Recent Advances in Multi-Material Micro- and Nano-Manufacturing, Int. J. Adv. Manuf. Technol., 47 (1-4), 161-180 (DOI: 10.1007/s00170-009-2214-5)
104. Chiesa-Estomba C. M., González-García J., Sistiaga-Suarez J. A., González Fernández I., (2022), A Novel Computer-Aided Design/Computer-Aided Manufacturing (CAD/CAM) 3D Printing Method for Nasal Framework Reconstruction Using Microvascular Free Flaps, Cureus, 14 (9) (DOI: 10.7759/cureus.28971)
105. Karakurt I., Aydoğdu A., Çıkrıkcı S., Orozco J., Lin L., (2020), Stereolithography (SLA) 3D Printing of Ascorbic Acid Loaded Hydrogels: A Controlled Release Study, Int. J. Pharm., 584 119428 (DOI: 10.1016/j.ijpharm.2020.119428)
106. Laxmi V., Joshi S. S., Agrawal A., (2020), Design Evolution and Performance Study of a Reliable Platelet-Rich Plasma Microdevice, Ind. Eng. Chem. Res., 59 (46), 20515-20526 (DOI: 10.1021/acs.iecr.0c03590)
107. Purvis N. B., Giorgio T. D., (1991), The Effects of Elongational Stress Exposure on the Activation and Aggregation of Blood Platelets, Biorheology, 28 (5), 355-367 (DOI: 10.3233/BIR-1991-28501)